NASA/TP-1999-209138

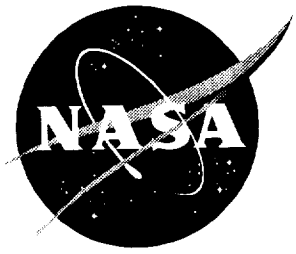

Experimental and Computational Investigation of a Translating-Throat, Single-Expansion-Ramp Nozzle

Karen A. Deere and Scott C. Asbury
Langley Research Center, Hampton, Virginia

National Aeronautics and
Space Administration

Langley Research Center
Hampton, Virginia 23681-2199

May 1999

Available from:

NASA Center for AeroSpace Information (CASI)
7121 Standard Drive
Hanover, MD 21076-1320
(301) 621-0390

National Technical Information Service (NTIS)
5285 Port Royal Road
Springfield, VA 22161-2171
(703) 605-6000

Contents

Summary

An experimental and computational study was conducted at low nozzle pressure ratios (NPR's) of a high-speed, single-expansion-ramp nozzle (SERN) concept designed for efficient off-design performance. In an effort to maximize nozzle performance, the throat is translated to different axial locations to provide a variable expansion ratio and allow a more optimum jet exhaust expansion at various flight conditions. Three throat locations (expansion ratios) were investigated to simulate the operation of this concept at subsonic-transonic, low supersonic, and high supersonic flight conditions.

The experimental study was conducted in the Langley Jet Exit Test Facility. Internal (static) nozzle performance was obtained at NPR's up to 13 for a low Mach number, an intermediate Mach number, and a high Mach number nozzle configuration with design nozzle pressure ratios near 9, 42, and 102. Two expansion-ramp surfaces, one concave and one convex, were tested for each nozzle. Paint-oil flow and focusing schlieren flow visualization techniques were utilized to acquire additional flow data at selected NPR's.

The Navier-Stokes code, PAB3D, was used with a two-equation k-ε turbulence model for the computational study. Nozzle performance characteristics were predicted at NPR = 5, 9, and 13 for the concave ramp, low Mach number nozzle and at NPR = 102 for the concave ramp, high Mach number nozzle. Qualitative comparisons with experimental results were obtained at nozzle pressure ratios of 10 and 13 for the concave ramp, high Mach number nozzle.

The initial experimental and computational results of the translating-throat SERN concept indicated some promising performance benefits. The experimental results indicate that the concave ramp, low Mach number nozzle had the highest axial thrust ratio over the test NPR range and had small values of resultant pitch thrust-vector angle at the design condition. Computational solutions verified the axial thrust ratio performance with predicted values within 1.5 percent of experimental data. Translating the throat of the SERN from a large expansion ratio to a small expansion ratio provided a more optimum expansion for the flow at low NPR's. In general, the nozzles with the concave ramp surface outperformed their convex ramp surface counterparts. The plume shear layer, oblique shock system, and separation from the external expansion ramp were observed in both the density gradients along the nozzle centerline and in the predicted Mach contours.

Introduction

Over many years, the advancement of exhaust nozzle technology has paralleled the development of gas turbine engines in the endless quest to fly faster and higher than current technology allows. The earliest gas turbine engine exhaust system, used in aircraft such as the F-80B, was a simple engine discharge control valve. With the addition of afterburning (AB) capability to gas turbine engines in the late 1940's, it became necessary to add variable geometry to exhaust nozzles. Variable geometry provides the larger exit area necessary for increased volumetric flow rate of the gas stream during the AB operation. This action prevents any increase in back pressure that would slow the airflow through the engine and cause the engine to stall (ref. 1). The first production supersonic fighter, the F-100D, used a two-position convergent nozzle. The F-101B incorporated a fully variable convergent nozzle to maintain maximum performance over a wide range of flight conditions.

The convergent-divergent (CD) nozzle was introduced in the 1950's in an effort to further increase the Mach number capability of military fighter aircraft. The addition of a divergent section to a convergent nozzle provided further expansion of the flow to supersonic conditions at the nozzle exit; this resulted in an increase in momentum thrust. Convergent-divergent nozzles often incorporate variable geometry to maintain high performance over a wide range of flight conditions. The F-4 represented the first proof of concept for the CD nozzle; now CD nozzles are utilized in most supersonic military aircraft.

Nozzle design improvements continued throughout the 1960's and 1970's with an emphasis on increased installed thrust. The nonaxisymmetric convergent-divergent nozzle was envisioned late in this period, with prospects of installed performance gains over the axisymmetric nozzles employed in aircraft such as the F-14 and F-15. As a result of improved nozzle integration with the airframe, the

nonaxisymmetric nozzle offers performance gains from a reduction in aft-end drag (ref. 2). Nonaxisymmetric designs also offer the designer additional freedom to integrate vectoring and reversing hardware into the nozzle.

Future high-speed aircraft capable of fulfilling a variety of missions may include military fighter-bomber aircraft in the Mach 4 regime, military or commercial transports in the Mach 5 regime, long-range cruisers in the Mach 10 regime, and single- or multiple-stage-to-orbit aerospace planes (ref. 3). These vehicles will require a highly integrated propulsion system and airframe (fig. 1). Although it is necessary for the propulsion system (inlet, engine, ejector, and exhaust nozzle) to be highly integrated with the airframe, the emphasis of this study is on the exhaust nozzle.

The exhaust nozzle of future high-speed vehicles will encounter large variations in back pressure over the flight regime. Generally, these variations are handled with a variable area nozzle that adjusts the exit area to the change in back pressure. However, for high-speed aircraft that encounter conditions where nozzle pressure ratio (ratio of jet total pressure to ambient pressure) reaches 600, variable geometry nozzles are impractical because of mechanical limitations that limit extreme variations in expansion ratio (refs. 4 to 6). Therefore, the designer is faced with improving the exhaust system performance of high-speed vehicles at off-design conditions while staying within existing mechanical limitations.

Studies to determine potential candidates for future high-speed aircraft exhaust systems have included performance comparisons of axisymmetric nozzles, single-expansion-ramp nozzles (SERN's) and two-dimensional convergent-divergent (2DCD) nozzles (refs. 4 to 6). All three nozzle candidates achieve satisfactory performance levels with a fixed geometry at on-design conditions; however, it is crucial to the development of a high-speed aircraft to determine which nozzle candidate performs best at off-design conditions.

The single-expansion-ramp nozzle is a variable area, nonaxisymmetric nozzle with a unique installation advantage for future high-speed vehicles because the underside of the vehicle's afterbody can be used for the external expansion ramp of the nozzle. The SERN may have additional advantages over axisymmetric or 2DCD nozzles, which include a reduction in weight and skin friction drag because of the short lower cowl.

Studies indicate that SERN's with one fixed design point, like most fixed geometry nozzles, suffer significant performance penalties at off-design conditions because of changing expansion ratio requirements (ref. 7). Although the performance peak for a SERN tends to cover a broader range of conditions as a result of an internal and external expansion process, a fixed design point (fixed expansion ratio) SERN still cannot perform well at far off-design conditions. The internal expansion process occurs between the nozzle throat and the trailing edge of the cowl, whereas the external expansion process occurs along the vehicle's lower afterbody surface (expansion ramp). Therefore, the maximum propulsive efficiency of SERN's is highly dependent on nozzle pressure ratio and nozzle expansion ratio (refs. 8 to 11). High-speed SERN's are designed with a large expansion ratio necessary for maximum performance at high speeds and altitudes. However, at subsonic, transonic, and low supersonic flight conditions, the expansion ratio is too large to maintain attached, fully expanded flow along the entire length of the expansion ramp. Consequently, the flow overexpands and separates from the expansion-ramp surface. Additionally, vortical flow may roll over the sidewalls, creating low-pressure regions along the ramp. These unfavorable conditions result in decreased nozzle thrust, increased afterbody pressure drag, and increased vehicle trim requirements to abate the large moments produced along the vehicle's lower afterbody surface.

The objective of this study was to investigate a translating-throat SERN concept, designed to improve the off-design performance of SERN, at low nozzle pressure ratios. Translating the axial location of the throat produces a nozzle with a variable expansion ratio by changing the exit area. This effort to maximize nozzle performance allows for a more optimum exhaust expansion at various flight conditions. An illustration of the translating-throat SERN concept designed for high performance at three Mach number ranges is shown in figure 2. To improve nozzle performance at off-design conditions, three actuated doors are integrated into the vehicle's lower afterbody

surface (expansion ramp) to provide a variable expansion ratio. In this illustration, a turbofan engine with a drop-down inlet is utilized for propulsion during low-speed flight conditions. For takeoff and low Mach number operation at subsonic and transonic flight conditions, door 1 opens to divert the flow internally to a throat location near the end of the long external expansion ramp. This diversion of flow yields the relatively small expansion ratio necessary for optimum expansion at low operating NPR's. As the vehicle gains speed and altitude in the low supersonic flight regime, door 1 closes and door 2 opens at the mid throat location to provide a larger expansion ratio as NPR increases. At high supersonic flight conditions, door 2 closes and door 3 opens to form the larger expansion ratio necessary for optimum performance at high operating NPR's. At even higher speeds, the gas turbine engine is shut off, all three doors are closed, and the vehicle uses a ramjet or scramjet engine for propulsion. The three doors remain closed for high-speed cruise operation, and the underside of the vehicle aft end acts as a fixed expansion ramp. This concept could be adapted to different engine configurations and designed to include more than three Mach number ranges.

Although the vehicle aeropropulsive performance was not the focus of this study, the external expansion-ramp surface must be designed with care so that vehicle performance does not suffer as a trade-off for nozzle internal performance improvements. The aeropropulsive performance is degraded by boattail drag when low pressure, from either accelerated or separated external flow, acts on an aft-facing surface such as the cowl. For this translating-throat SERN concept, boattail drag may result from large boattail angles required to divert the flow internally at low and intermediate Mach numbers.

This publication discusses an experimental and computational investigation of the translating-throat SERN concept. The experimental study was conducted in the Langley Jet Exit Test Facility. A sketch of the experimental model representing the translating-throat SERN is shown in figure 3. Three nozzles designed for high performance at low (door 1), intermediate (door 2), and high (door 3) Mach number ranges were investigated. Two expansion-ramp surfaces, one concave and one convex, were tested for each nozzle to determine which geometry provided a better surface for attached, expanding flow along the upper expansion ramp. The internal nozzle performance of the six nozzles (table 1) was obtained at nozzle pressure ratios from 2 to 13. Paint-oil flow and focusing schlieren flow visualization techniques were used at selected NPR's to obtain additional information about the flow expansion along the expansion ramp.

The Navier-Stokes code PAB3D with a k-ε turbulence model was used for the computational study. For quantitative and qualitative comparisons with experimental results, a two-dimensional computational domain was used to predict internal nozzle performance at NPR's of 5, 9, and 13 for the concave ramp, low Mach number nozzle and at NPR's of 10, 13, and 102 for the concave ramp, high Mach number nozzle.

This publication includes a discussion of computational fluid dynamics (CFD) and experimental results and presents predicted flow characteristics compared with data obtained from the paint-oil flow and focusing schlieren flow visualization techniques.

Symbols

A_e	nozzle exit area, in^2
A_t	nozzle throat area, in^2
B_r	estimated uncertainty of data reduction equation r
$B_1,...,B_J$	estimated uncertainty of measurements used to determine r
C_d	discharge coefficient, $\frac{w_p}{w_i}$
$\mathbf{F}$	total body force vector (eq. (4))
F_A	measured thrust along body axis, lbf
F_A/F_i	axial thrust ratio
$\mathbf{F}_{fric}$	total skin friction force vector, lbf
F_i	ideal isentropic gross thrust (eq. (1)), lbf
F_N	measured jet normal force, lbf

F_r	resultant gross thrust, $\sqrt{F_A^2 + F_S^2 + F_N^2}$, lbf
F_r/F_i	resultant thrust ratio
F_S	measured jet side force, lbf
f_μ	damping function, $\exp\left[\frac{-3.41}{1 + (R_t/50)}\right]$
g	gravitational constant, $1g \approx 32.174$ ft/sec^2
h_e	height at nozzle exit (fig. 8(a)), in.
h_t	height at geometric minimum area (fig. 8(a)), in.
k	turbulent kinetic energy, Pa
L	reference length of nozzle assembly (fig. 8(a)), 16.9 in.
l_c	length of cowl (fig. 8(a)), in.
l_r	axial length of ramp from cowl exit to ramp trailing edge (fig. 8(a)), in.
M	free-stream Mach number
N	unit normal vector, n_1, n_2, n_3
NPR	nozzle pressure ratio, $\frac{p_{t,j}}{P_a}$
NPR_D	design nozzle pressure ratio based on external expansion ratio
$NPR_{D,int}$	design nozzle pressure ratio based on internal expansion ratio
P1,...,P29	pressure orifice number (fig. 9)
p	ramp static pressure, psi
p_a	ambient pressure, psi
$p_{t,j}$	jet total pressure, psi
p_∞	free-stream static pressure, psi
R	universal gas constant, 53.3 ft-lbf/lbm-°R
R_T	turbulent Reynolds number
r	data reduction equation
$T_{t,j}$	average jet total temperature, °R
U	velocity vector
u	velocity component in x direction
w_i	ideal weight-flow rate (eq. (3)), lbf/sec
w_p	measured weight-flow rate, lbf/sec
x	axial orifice location (fig. 9), in.
x_t	axial location of geometric throat from nozzle connect station (fig. 8(a)), in.
y	spanwise orifice location (fig. 9), in.
y^+	law-of-the-wall coordinate, $\frac{n\sqrt{\rho_w \tau_w}}{\mu_w}$
α	angle of attack, deg
γ	ratio of specific heats, 1.3997 for air
δ_p	resultant pitch thrust-vector angle (eq. (2)), deg
ε	turbulent energy dissipation
θ_r	estimated ramp angle (fig. 8(a)), deg
μ	laminar viscosity
μ_T	turbulent viscosity
μ_w	local laminar viscosity at wall
ρ	density, slug/ft^3
σ	standard deviation (table 2)

τ_w wall shear stress, $\mu \left.\frac{\partial u}{\partial n}\right|_w$

ϕ_r initial ramp angle at throat (fig. 8(b)), deg

Subscripts:

ext external

int internal

w wall

Abbreviations:

AB afterburning

CD convergent-divergent

CFD computational fluid dynamics

ESP electronically scanned pressure

MS model station, in.

RANS Reynolds averaged Navier-Stokes

SERN single-expansion-ramp nozzle

2D two-dimensional

3D three-dimensional

Apparatus and Procedures

Test Facility

The experimental study was conducted in the Langley Jet Exit Test Facility (JETF). This facility is used to test the internal performance of nozzles by simulating propulsion flows at static (wind-off) conditions. The JETF test apparatus consists of a propulsion simulation system, two independently controllable air supply systems, and a data acquisition room. The air systems use the same clean, dry air supply used in the Langley 16-Foot Transonic Tunnel, and the same valves, filters, and heat exchanger are used to provide air at a constant total temperature near 530°R. The model is mounted on the propulsion simulation system in a soundproof room with an air exhaust collector duct downstream of the jet.

Propulsion Simulation System

The translating-throat SERN model was tested on a dual-flow, single-engine, propulsion simulation system. A photograph (looking upstream) of the high Mach number nozzle mounted on the propulsion system in the Langley Jet Exit Test Facility is shown in figure 4, and a sketch (side view) of the propulsion system attached to a structural cart is shown in figure 5. Independently controlled primary and secondary flow systems provided pressurized air to isolated plenum chambers on the propulsion system through two pairs of semirigid, thin-walled (0.021-in. wall thickness), 1-in-diameter, S-shaped, stainless steel tubes (S-tubes). These tubes were designed to minimize balance tares caused by flexure of the S-tubes as air pressure is increased or by the transfer of axial momentum as air is transferred from the nonmetric to the metric part (supported by the force balance) of the system. This design provides repeatable force and moment tares so that the final data reflect only forces and moments produced by the nozzle. The primary and secondary air systems can be used separately or combined for dual-flow operation. The two independent flow streams each passes through a multiple critical venturi system (ref. 12) where the flow rate of each stream is measured to within a 0.1-percent measurement uncertainty. For the current investigation, only the primary air system was used.

The air supplied to the propulsion system is discharged radially from the primary plenum into an annular low-pressure duct (on the model centerline) through eight equally spaced sonic nozzles. The airflow then passes over an aerodynamic balance fairing and through an axisymmetric choke plate (located just downstream of MS 14.75), that provides a pressure drop to ensure a uniform flow field. Downstream of the choke plate, the air passes through the axisymmetric primary instrumentation section at MS 17.75 and then through the circular-to-rectangular transition section at MS 24.25. A second choke plate at MS 30.25 is located downstream of the transition section to ensure a uniform flow field in the SERN instrumentation section. The airflow enters the SERN at MS 36.25 and is

then exhausted to atmospheric conditions in a test bay with louvered ceiling vents to channel the flow outside the facility. A sketch of the installation of a typical translating-throat SERN on the propulsion simulation system is shown in figure 6.

Experimental Model

Each nozzle configuration included a ramp assembly, a ramp insert, a cowl, and two sidewalls. A photograph of the model hardware is shown in figure 7. The geometric parameter and the design nozzle pressure ratio NPR_D of each nozzle are listed in table 1, and each geometric parameter is illustrated in figure 8(a). Three cowl pieces of different lengths were used to simulate changing the throat location of the translating-throat SERN concept. The throat locations, door 1, door 2, and door 3, provided three expansion ratios for the subsonic-transonic (low Mach number) portion, the low supersonic (intermediate Mach number) portion, and the high supersonic (high Mach number) portion of the flight envelope, respectively. Two expansion-ramp surfaces, one concave and one convex, were tested at each throat location by interchanging ramp inserts.

The ramp assembly was common for all nozzles and was 16.9 in. long. Each ramp insert began at $x = 4.6$ in. and was 10.88 in. long. The nozzles had a rectangular cross section with a nominal throat area of 2 in^2 and a width of 5 in. The overall expansion angle θ_r and initial expansion angle ϕ_r are listed in table 1. The overall expansion angle is defined as the angle between a horizontal line drawn from the ramp at the throat location and a segment drawn from the throat location to the trailing edge of the ramp (fig. 8(a)). The initial expansion angle is defined for the ramp geometry in the immediate vicinity of the throat as the angle between a horizontal line drawn from the ramp at the throat location and the local ramp surface as illustrated in figure 8(b).

Instrumentation

A six-component strain-gauge balance located on the centerline of the propulsion simulation system was used to measure the forces and moments acting on the model. This balance measures up to ±800 lbf of normal force, ±1200 lbf of axial force, and ±12 000 in-lbf of pitching moment. Negligible measurements were expected from side force, rolling moment, and yawing moment because of model symmetry.

A calibrated multiple critical venturi (ref. 12), located upstream of the S-tubes, was used to determine the weight-flow rate of the high-pressure air supplied to the test nozzle. One total temperature and three static pressure measurements taken upstream of the venturi and one static pressure measurement taken downstream of the venturi were used in the calculation of weight-flow rate. Pressures were measured with 2000-psia transducers, and the temperature was measured with a platinum resistance thermometer.

In the primary instrumentation section, jet total pressure was measured with a nine-probe rake aligned along a diagonal, and jet total temperature was measured with two thermocouples. In the SERN instrumentation section, jet total pressure was measured with two five-probe rakes that were aligned vertically, and jet total temperature was measured with one thermocouple located at the same model station as the probe rakes. Because of the expected pressures in the instrumentation section, 250-psid transducers were used to obtain the most accurate total pressure measurements. The test nozzles were connected to the SERN's instrumentation section at MS 36.25 (designated $x = 0$). Twenty-nine static pressure orifices were located along the upper ramp surface of each configuration. The geometric locations and coordinates of the static pressure orifices are shown in figure 9. A rack-mounted, 250-psi, electronically scanned pressure (ESP) module was used to measure static pressures along the expansion ramp.

The estimate of balance accuracy is shown in engineering units and as a percent of full scale in table 2. The estimated accuracies of gauge transducers, thermocouples, and the ESP module are listed in table 3.

Focusing Schlieren Flow Visualization

The optical specifications for the focusing schlieren system used in this experiment were determined from the requirements defined in reference 13. The visualization system, shown in figure 10, was used to determine the density gradients along a 2D field of view. The longitudinal field-of-view dimensions were 13 by 17 in. with a 0.2-in. depth of sharp

focus. By monitoring the field of view from the data acquisition room, flow characteristics at specific data points were selected and recorded with a still camera.

Paint-Oil Flow Visualization

Paint-oil flow visualization is helpful in determining 2D and 3D flow patterns along the nozzle surfaces and is an excellent aid for interpreting pressure and force data. The paint-oil flow mixture used in this study was comprised of kerosene, linseed oil, dry paint, and oil paint. A thick, heavy paint mixture was necessary for capturing flow characteristics from supersonic jet flows.

The procedure was initiated by setting the required NPR from the data acquisition room. Once a steady-state flow condition was reached, a supply valve for the system was closed to stop the airflow and allow the paint-oil mixture to be applied to the expansion ramp of the nozzle. With the paint mixture applied, the supply valve was opened and the selected flow condition was achieved within seconds. This process was established so that minimal start-up flow characteristics would be present in the flow patterns. The selected flow condition was held for approximately 20 sec to allow the paint to dry and to record data at the selected flow condition.

Data Reduction

Each data point was generated from the average of 50 samples of data recorded at a rate of 10 samples/sec. The data were further reduced and corrected according to the data reduction procedures presented in reference 14. Data from all instrumentation systems were recorded simultaneously. Three basic internal performance parameters were used in the discussion of results: axial thrust ratio F_A/F_i, resultant pitch thrust-vector angle δ_p, and discharge coefficient C_d.

Axial thrust ratio, which is a measure of nozzle thrust efficiency, is defined as the ratio of measured axial force along the body axis to ideal thrust. The measured axial force along the body axis is used to compute the axial thrust ratio F_A/F_i. Ideal thrust is calculated by assuming one-dimensional isentropic expansion from the stagnation conditions in the instrumentation section as follows:

$$F_i = w_p\sqrt{\frac{2\gamma RT_{t,j}}{g(\gamma-1)}}\sqrt{1-\left(\frac{p_{t,j}}{p_a}\right)^{(1-\gamma)/\gamma}} \quad (1)$$

The resultant thrust ratio is the ratio of gross thrust to ideal thrust. Gross thrust is determined by calculating the square root of the sum of the squares of measured normal, side, and axial forces. The axial thrust ratio is examined in this investigation because it accounts for losses that result from flow being vectored away from the axial direction, and the resultant thrust ratio does not. The axial and resultant thrust ratios are equivalent when the jet-exhaust flow is unvectored and the resultant pitch thrust-vector angle δ_p is zero. Nonzero values of δ_p occur when the flow is vectored away from the axial centerline. The resultant pitch thrust-vector angle is determined as follows:

$$\delta_p = \tan^{-1}\frac{F_N}{F_A} \quad (2)$$

Large normal force variations usually result in nonlinear variations of δ_p as a function of NPR. The variations in normal force also correspond to significant pitching moments that increase the trim requirements of SERN.

The discharge coefficient C_d is the ratio of the measured weight-flow rate to the ideal weight-flow rate; values less than 1.0 are expected. Ideal weight flow is calculated by assuming isentropic choked flow in a convergent nozzle as follows:

$$w_i = A_t P_{t,j}\left(\frac{2}{\gamma+1}\right)^{(\gamma+1)/2(\gamma-1)}\left(\frac{\gamma g}{RT_{t,j}}\right) \quad (3)$$

Ideal weight flow is a function of total pressure, total temperature, and nozzle throat area. Weight-flow losses are attributed to viscous and vena contracta effects (ref. 15) at the throat of the nozzle. The vena contracta effect occurs when inertial forces cause the flow near the wall to overshoot the convergent-divergent transition at the throat of the nozzle. The overexpansion of the flow at the throat can result in shocks just downstream of the throat as the flow is recompressed.

Force and moment measurements were corrected for model weight tares, isolated balance-component interactions, jet-off installation tares, and installed pressure and momentum tares determined from pretest calibrations. Figure 11 shows a typical hardware set-up for the balance calibrations on the propulsion simulation system. Balance calibrations were conducted prior to the test to determine propulsion tares resulting from bridging the nonmetric and metric portions of the propulsion system with the S-tubes. S-tube pressurization and axial momentum tares were then determined by testing single-engine Stratford choke calibration nozzles with known performance over ranges of internal pressure and external forces and moments expected during the actual experiment. A range of calibration nozzles was tested to determine the effect of nozzle throat area. Reference 16 describes the balance calibration process in more detail.

The accuracy of the balance and the pressure transducers was used to estimate the uncertainty of the calculated experimental performance quantities. The individual uncertainty contributions to a performance quantity were estimated with a first-order Taylor series expansion. The final uncertainty of the performance quantity was obtained from a root sum square of the individual contributions. This method, described in reference 17, was used to estimate the uncertainty of axial thrust ratio, discharge coefficient, and resultant pitch thrust-vector angle and is summarized in the appendix.

Computational Code and Procedures

Navier-Stokes Equations

The PAB3D code solves the three-dimensional, time-dependent, Reynolds averaged Navier-Stokes (RANS) equations and uses one of several turbulence models for closure of the RANS equations. The governing equations are solved in generalized coordinates and in conservative form. The simplified, thin-layer Navier-Stokes equations are implemented into PAB3D in an effort to decrease computational requirements. This approximation neglects derivatives in the viscous terms streamwise and parallel to the surface because they are typically negligible in comparison with the derivatives normal to the surface. Extensive details of PAB3D are found in references 18 and 19.

The flow solver was written with three numerical schemes: the flux vector-splitting scheme of Van Leer (ref. 20), the flux difference-splitting scheme of Roe (ref. 21), and a modified Roe scheme primarily used for space marching solutions. Each method uses the finite volume principle to balance the fluxes across grid cells and the upwind biased scheme of Van Leer or Roe to determine fluxes at the cell interfaces. Only the inviscid terms of the flux vectors were split and upwind differenced, whereas the diffusion terms of the Navier-Stokes equations were centrally differenced.

Typical three-dimensional solutions are developed with the Van Leer and Roe schemes. An iteration to steady state in a 3D computational domain includes a forward and backward relaxation sweep in the streamwise direction while implicitly updating each cross plane. In a 2D computational domain, an index swapping technique is used to speed convergence. Since the cross plane contains only one cell in a 2D computational domain, the streamwise plane is swapped with the cross plane to eliminate the forward and backward relaxation sweep and to obtain a fully implicit domain. This procedure typically increases the rate of convergence and decreases the computational space and time required to obtain a converged solution.

Turbulence Model

Turbulence modeling is required to predict accurate solutions for many flow fields. The PAB3D code can perform several turbulence simulations by implementing either an algebraic or a linear or nonlinear, two-equation turbulence model. An algebraic, two-layer Baldwin-Lomax model is accurate for simple viscous flows because the turbulent viscosity μ_T is determined by a local function. A two-equation k-ε model with second-order closure is used to model more complex viscous flow features such as shear layers and regions of separated flow. A second equation is used to solve for the turbulent length scale in addition to the equation for turbulent kinetic energy k. Because the k-ε model has a singularity at solid surfaces, either a damping function or a wall function must be implemented to adjust the turbulent viscosity μ_T near these surfaces. The grid in the boundary layer at wall surfaces must be well-defined with a law-of-the-wall coordinate y^+ of approximately 2 for adequate modeling of the boundary layer flow (ref. 19).

Based on past experience with the PAB3D code (ref. 19) and the expectation of separated flow regions in the present solutions, a two-equation k-ε turbulence model was chosen for solving the internal nozzle flow and jet plume development in this investigation. The k and ε transport equations were written in conservative form and were solved uncoupled from the Navier-Stokes equations to decrease computational requirements. A modified Jones and Launder form (ref. 22) of the damping function f_μ was utilized to treat the singularity at the wall because separated flow regions along the expansion ramp were expected at overexpanded conditions. A high Reynolds number model with no damping function was implemented in the free-stream blocks.

Performance Calculations

A performance package (ref. 23) is included in the PAB3D code to aid in determining solution convergence and to calculate nozzle or aerodynamic performance parameters. Quantities such as lift, drag, thrust, moments, heat transfer, and skin friction may be computed for many complex geometric configurations and multistream flows. A small control file allows the user to define the control volume or volumes of interest.

The momentum theorem is applied to the user-defined control volume to determine the momentum and pressure forces on the model. The total body force vector $\mathbf{F}$ is defined as

$$\mathbf{F} = \Sigma[\rho\mathbf{U}(\mathbf{U}\cdot\mathbf{N}) + (p - p_\infty)\mathbf{N}]\Delta A + \mathbf{F}_{\text{fric}} \quad (4)$$

where ΔA is the cell face area and $\mathbf{N}$ is the cell face unit vector. To determine a cell solid surface static pressure, the cell-centered static pressure is interpolated to the surface where the velocity is assumed to be zero. As a solution converges, $\mathbf{U}\cdot\mathbf{N}$ goes to zero at solid surfaces.

The skin friction force $\mathbf{F}_{\text{fric}}$ is calculated with only the velocity gradients normal to the nozzle surface contributing to the velocity term of the viscous stress tensor. A two-point difference is used to determine the velocity gradients, with one zero-magnitude velocity vector at the surface and another at the cell center. Sutherland's formula (ref. 24) is used to calculate the laminar viscosity at the surface. The static temperature at a local cell center is extrapolated to the surface, and a reference viscosity and temperature condition are used. Momentum and pressure forces are calculated at user-defined intervals so that performance quantities may be monitored throughout the development of a solution.

Computational Grid

The computational domain for PAB3D consists of a general multiblock grid topology with multiple-to-one or arbitrary, conservative patching between the block interfaces, which is necessary for modeling complex configurations. An algebraic grid generator is used in this investigation to generate two computational multiblock grids that represent the low and high Mach number experimental nozzles with the concave expansion-ramp surface. Both grids are two-dimensional and are described in more detail in the following sections.

Low Mach Number Nozzle Grid Definition

The complete computational domain of the concave ramp, low Mach number nozzle and a close-up view of the grid density at the nozzle throat and expansion ramp are shown in figure 12. The internal duct and the expansion ramp are defined with the design coordinates of the nozzle model hardware. The grid block that defines the throat and external expansion ramp has dimensions of 161 by 85 (streamwise by normal). The first cell in the boundary layer along the inside of the nozzle and along the ramp is defined for $y^+ < 2.5$ at the coarse mesh level to ensure the development of turbulence in the solutions. The computational domain consists of 16 blocks. The far-field boundary is located 106 throat heights (12.6 ramp lengths) downstream of the nozzle exit, the lower lateral boundary is located 88 throat heights (10.6 ramp lengths) below the expansion ramp, and the upper lateral boundary is located 52 throat heights (6.2 ramp lengths) above the expansion ramp.

High Mach Number Nozzle Grid Definition

The complete computational domain for the concave ramp, high Mach number nozzle and a close-up view of the grid density at the nozzle throat and expansion ramp are shown in figure 13. The blocks that defined the throat region and the external expansion ramp have dimensions of 161 by 85. As for the

computational domain of the low Mach number nozzle, the first cell in the boundary layer is defined for $y^+ < 2.5$ at the coarse mesh level. The computational domain consists of 20 blocks. The far-field boundary is located 206 throat heights (8.8 ramp lengths) downstream of the nozzle exit and the upper and lower lateral boundaries are located 180 throat heights (7.75 ramp lengths) away from the expansion ramp.

Grid Mesh Sequencing

A mesh sequencing procedure was utilized to accelerate grid convergence and to determine the grid sensitivity of the performance quantities and of the normalized static pressure distributions on the expansion-ramp surface. The solution was initially developed on a coarse mesh that contained one half the grid points of the fine mesh in the streamwise and cross-stream directions. Once the solution converged on the coarse mesh, it was interpolated to a medium mesh that included one quarter more of the grid points in both directions. After convergence was obtained on the medium mesh, the solution was refined and converged on the fine mesh. The grid sensitivity results are shown in the section "Experimental and Computational Comparisons."

Boundary Conditions

The code offers five types of boundary conditions that may be applied to different regions of the computational domain. Riemann invariants along characteristics were used for the lateral free stream and free-stream inflow boundaries. Fixed total temperature and total pressure were used for the nozzle inflow boundary. At the far-field outflow boundary, a constant static pressure for subsonic flow was used because the simulations were calculated with a static free stream. The boundary condition implemented on solid surfaces was a no-slip adiabatic wall condition used for viscous solutions.

Experimental and Computational Approach

The experimental nozzles were tested through a range of NPR from 2 to 13. The experimental test range of NPR was typical of the operating conditions for the low Mach number nozzles. The intermediate and high Mach number nozzles were highly overexpanded at all test conditions.

A 2D domain was used for the computational investigation. This approach to modeling the SERN geometry provided information about the flow characteristics along the centerline and a good estimate of performance quantities near the design condition when minimal separation occurred. At highly overexpanded conditions, 3D flow separation (observed in the experiment) would not be modeled with a 2D domain, and CFD would overpredict thrust efficiency.

CFD was used to simulate the concave ramp, low Mach number nozzle at NPR's of 5, 9, and 13 with an approximately static free stream ($M = 0.05$). To aid the stability of the code, a small, convective free-stream Mach number is usually implemented when simulating static conditions. Two solutions at highly overexpanded conditions (NPR = 10 and 13) were computed for the concave ramp, high Mach number nozzle in an effort to compare internal performance with the experimental results. Qualitative solutions were obtained, but the simulations were not fully converged because of the large region of separated flow along the ramp at overexpanded conditions. A higher external free stream ($M = 0.1$) was used for the high Mach number nozzle in an effort to obtain stable solutions at the highly overexpanded conditions, which should have minimal effect on the qualitative comparisons. The high Mach number nozzle was also simulated at the on-design condition ($NPR_D = 102$). Predicted performance quantities were compared with the experimental data, and when applicable, predicted flow characteristics were compared with paint-oil flow and focusing schlieren flow visualization.

A grid mesh and solution convergence study was conducted for each computational simulation. The grid mesh sequencing scheme was used to estimate the dependence of the solution on the mesh density of the computational domain. A solution performance and residual history were used to monitor convergence as the solution developed at each grid level. The main convergence criteria were to obtain variations in axial thrust ratio and discharge coefficients of less than 0.001 over 1000 iterations. Secondary convergence criteria were to obtain a drop in the residual of 2 orders of magnitude.

Discussion of Results

Single-expansion-ramp nozzles may be internally convergent or internally convergent-divergent, which affects performance because expansion of the exhaust flow either occurs externally or internally and externally, respectively. For an internally CD SERN, the internal expansion is contained by the nozzle surface upstream of the cowl trailing edge and is defined by the internal expansion ratio $(A_e/A_t)_{int}$; the external expansion occurs downstream of the cowl trailing edge between a free (ambient-exhaust) boundary and the upper ramp and is defined by the external expansion ratio $(A_e/A_t)_{ext}$. Internally CD SERN's generally exhibit two peaks in thrust performance over a broad range of NPR because the exhaust flow expansion process occurs both internally and externally (ref. 11).

Because the external exhaust flow expansion has a free (ambient-exhaust) boundary, aeropropulsive performance for SERN is a function of NPR, M, and α. In this static investigation, the internal performance parameters depend on NPR only. Generally, $\delta_p = 0°$ for a well-designed SERN operating at the design condition because the thrust would have been designed to align in the axial direction. At off-design conditions, large nonlinear values of δ_p with respect to NPR occur because the expansion-ramp surface has no opposing surface to balance the forces of the expanding flow. The unopposed surface can inhibit the performance of SERN's because the requirement to trim aircraft pitching moments can result in large drag penalties. Additionally, a reduction in body axis thrust occurs at nonzero values of δ_p.

Effect of Throat Location

The effect of throat location on internal performance of the concave ramp nozzles is shown in figure 14. All three concave ramp nozzle configurations had similar thrust ratio trends. Each nozzle configuration exhibited two peaks in axial thrust ratio and a fairly constant axial thrust ratio for NPR > 8.

The low Mach number nozzle with a design nozzle pressure ratio of 9 had the highest axial thrust ratio of the concave ramp configurations over the test range of NPR. The axial thrust ratio was between 0.5 and 4 percent lower for the intermediate Mach number nozzle operating in the same range of NPR. This behavior was expected because the intermediate Mach number nozzle with $NPR_D = 42.2$ was highly overexpanded in the test range of NPR. Not surprisingly, axial thrust ratio for the high Mach number nozzle was the lowest of the three in the same NPR range because it was operating farthest from its design point, $NPR_D = 102.4$. The resultant penalties in thrust noted previously result from overexpansion losses when the nozzles operate at off-design conditions. Separation along the ramp was more significant as the length of the ramp increased from 4.2 in. for the low Mach number nozzle to 11.6 in. for the high Mach number nozzle. At wind-on ($M > 0$) highly overexpanded conditions, the thrust penalties would most likely be more severe because the large separated region along the expansion ramp would generally result in higher afterbody pressure drag. To mitigate thrust penalties at wind-on conditions, care must be taken when designing the external cowl to ensure that the boattail angle promotes attached expanding flow (ref. 7).

The intermediate and high Mach number nozzles (higher design NPR's) had larger magnitudes of δ_p than the low Mach number nozzle at NPR = 9. Translating the throat from a high to a low expansion ratio would provide a decrease in vector angle of approximately 7° at NPR = 9. This result illustrates the benefit of translating the throat of the nozzle to achieve a more optimum expansion ratio for a given set of conditions, that is, a smaller expansion ratio at takeoff and subsonic flight conditions to eliminate unwanted pitch vectoring and to reduce vehicle trim requirements.

The effect of throat location on the performance of the convex ramp nozzles is shown in figure 15. Only general comparisons are made among the convex nozzles because model fabrication produced geometric differences at the throat. The intermediate Mach number nozzle had a small internal divergence, as shown in figure 8(b). The low and high Mach number nozzles had a positive initial expansion angle that appeared to vector the flow away from the expansion ramp.

The intermediate Mach number nozzle exhibited a higher axial thrust ratio than the low Mach number nozzle for NPR > 3.5, even though it was overexpanded throughout the test NPR range. The low Mach number nozzle had the highest axial thrust ratios for NPR < 3.5, probably because of the combination of an internally convergent geometry and a short external

expansion ramp. Even though the high Mach number nozzle also had an internally convergent geometry, thrust ratio was lower than for the low Mach number nozzle at NPR < 3.5, most likely caused by overexpansion losses that occurred along the longer external expansion ramp.

The convex ramp, low Mach number nozzle had a resultant pitch thrust-vector angle δ_p of 18.7° near the design point of NPR = 10 instead of 0, as would be expected from a well-designed SERN operating near the design point. The convex ramp, high Mach number nozzle had a large positive increase in δ_p of 14.5° from NPR = 3.75 to 4. At this change in NPR, the flow dramatically separated from the upper ramp surface and remained separated through NPR = 13, as illustrated in figure 16. The values and trend of δ_p for the convex ramp, intermediate Mach number nozzle were similar to those of the concave nozzles, all of which had negative initial expansion angles at the throat.

Effect of Ramp Geometry

The effect of ramp geometry on performance is shown in figures 17 to 19. The concave expansion ramp provided a better expansion surface for the flow; this resulted in much higher thrust ratios and smaller values of δ_p. All three nozzles with convex ramp surfaces had larger thrust ratios for NPR < 3, whereas the first peak in thrust ratio for the concave ramp surface nozzles occurred at NPR ≥ 3. (See figs. 17 to 19.) This result was expected because the convex ramp nozzles had internal expansion ratios of 1.01 or less, such that the nozzles basically had an internal geometry typical of a convergent nozzle with an internal design point NPR_D of 1.89. All the concave ramp nozzles had an internal expansion ratio greater than 1 with a slightly larger internal design NPR than the convex ramp nozzles; this resulted in the slight delay of peak thrust ratio until a higher NPR was reached. The low Mach number nozzle at $NPR_D = 9$ produced $\delta_p = 0°$ with the concave ramp surface because the thrust was aligned in the axial direction, whereas the convex surface vectored the thrust to produce $\delta_p = 17.5°$ (fig. 17(b)).

Experimental and Computational Comparisons

Low Mach Number Nozzle

Predicted and experimentally measured internal nozzle performance parameters, including axial thrust ratio, resultant pitch thrust-vector angle, and discharge coefficient, are shown in figures 20 and 21. Axial thrust ratio was predicted within 1.5 percent of the experimental data (fig. 20(a)). Overprediction of axial thrust ratio was expected from the CFD analysis because the highly complex 3D flow observed along the expansion ramp in the experiment and in previous studies (refs. 25 to 28) was simulated with a 2D computational domain. The 2D simulations accurately represent flow along the centerline of the nozzle, but the predicted performance quantities were calculated by assuming that the centerline flow solution was constant over the 5-in. width of the nozzle. Therefore, the 3D separation losses along the expansion ramp that were present in the experiment were not modeled with the 2D computational domain.

In general, PAB3D predicted both the level and the trend of resultant pitch thrust-vector angle δ_p as a function of NPR (fig. 20(b)). The calculation of δ_p from integrated pressures along the expansion ramp did not include the lateral variation of separated flow along the ramp because the computational domain was 2D. However, the absolute magnitudes of δ_p at selected NPR's were predicted within ±2.5° of the experimental data.

Predicted discharge coefficient and experimental discharge coefficient are shown as a function of NPR in figure 21. Experimental results indicate an increasing C_d up to 1.04 at NPR = 13. An unrealistic value of $C_d > 1.0$ indicates that the nominal throat area of the nozzle used for the experimental calculation of C_d was smaller than the actual throat area of the nozzle. Normally, C_d would level off to a constant value after the flow fully expanded internally at NPR = 1.89 (refs. 8 to 11). The increasing trend of experimental C_d indicates that the effective throat area was increasing with NPR and was greater than the nominal minimum area (used in the calculation of ideal weight flow in the experiment) when $C_d > 1$. An area greater than the nominal minimum area might occur from a skewed throat that is not aligned with the geometric minimum area, whereas the increasing area may result from the shifting of the skewed throat due to nonuniform boundary layer flow upstream of the geometric minimum area. It could also be due to "oil canning" of the cantilevered cowl. Unlike the nominal throat area used for the experimental calculation of C_d, the minimum area of the grid was used in the predicted solution, which ensures that C_d is less than 1. The decrease in

nozzle efficiency in passing weight flow as NPR increased from 9 to 13 may have resulted from excessive boundary layer thickness and nonuniform flow at the throat.

As shown in figure 22, the predicted normalized static pressure distribution along the centerline of the ramp was generally very good at NPR = 13. A sketch of the nozzle internal geometry is included in figure 22 to aid the reader in identifying geometric characteristics that impact flow characteristics. The throat of the nozzle is located near $x/L = 0.75$. The flow upstream of the throat is subsonic; thus, a decrease in static pressure upstream of $x/L = 0.28$ occurs as the area decreases. In the constant area section between $x/L = 0.28$ and 0.7, the predicted and experimental pressures remain approximately constant. The code predicts an overexpansion and compression at the throat, as expected from the large turning angle required at the throat discontinuity. A weak shock and an apparent induced flow separation are present near $x/L = 0.86$. The weak shock was not detected in the experimental data because of the limited number of orifices along the expansion ramp.

The overprediction in pressures between $x/L = 0.28$ and 0.7 coincides directly with the location of the ramp insert. The experimental pressure in this constant area region, $p/p_{t,j} = 0.85$, corresponds to $M \approx 0.487$. The predicted pressure in this region, $p/p_{t,j} = 0.89$, corresponds to $M \approx 0.411$. For the flow to have a lower predicted Mach number in the subsonic region upstream of the throat, the effective flow area in the fabricated nozzle must have been smaller than that of the nozzle design. The change of effective flow area could result from the model assembly and a thinner predicted boundary layer in the computational solution. The difference between predicted and experimental pressures correlates to a 13-percent change in effective flow area, which would result from a change in duct height of approximately 0.065 in. Because this pressure discrepancy occurred upstream of the nozzle choke location at the throat, it is not expected to have affected the performance or the flow characteristics along the expansion ramp.

The concave ramp, low Mach number nozzle with the near sidewall removed (fig. 23(a)) was included to more easily identify geometric features in the following discussion. Qualitative comparisons between the experimental density gradients along the centerline and the predicted Mach contours at NPR = 13 can be made from figures 23(b) and 24. The thick shear layer, the oblique shock system internal to the plume, and the shock-induced separation from the external expansion ramp are evident in both figures. The paint-oil flow pattern along the ramp at NPR = 13 is shown in figure 25. The thick line, normal to the flow direction, provided indication of shock-induced separation located near $x/L = 0.87$. The flow up to the separation line is essentially 2D, whereas the 3D pattern downstream of the separation line provides evidence of two symmetric vortex trails. Three-dimensional separation of this nature is not accounted for in the 2D CFD calculations.

A grid sensitivity study for the solution developed at NPR = 13 is included as a representative example of the evaluation of solution dependency on grid density completed for each computation. Performance quantities at each grid density level are shown in figure 26. The discharge coefficient changed 0.7 percent from the coarse to medium mesh refinement and was negligibly different at the fine mesh refinement. The axial thrust ratio changed 0.24 percent at the medium mesh refinement and 0.29 percent at the fine mesh refinement. The minimal changes in performance quantities among the various mesh densities indicate that the solution is minimally dependent on the number of grid points used to develop the solution.

The solution convergence history for the concave ramp, low Mach number nozzle simulation at NPR = 13 is shown in figure 27. The main convergence criteria, variations less than 0.001 in F_A/F_i and C_d over 1000 iterations, were met. The residual dropped 1.5 orders of magnitude on the coarse mesh but remained nearly constant on the medium and the fine meshes; this may be a consequence of the region of separated flow along the expansion ramp. Because the solution residual was based on all the blocks in the computational domain, regions of separated flow in one or more blocks may mask a decreasing residual in the rest of the blocks. This outcome has been observed in a previous study of a SERN with separated flow along the upper expansion-ramp surface (ref. 29). In such cases, the strict convergence criteria on performance parameters must be met.

High Mach Number Nozzle

The concave ramp, high Mach number nozzle shown in figure 28(a) had a design point NPR_D of

102.4; thus, the nozzle was overexpanded at NPR = 10 and 13. As a result, substantial 3D flow separation occurred along the ramp at all test conditions. In figure 28(b), photographs of paint-oil flow patterns along the ramp and density gradients along the centerline at NPR = 13 give good indication of separated flow. The thick line near $x/L = 0.44$ provided evidence of shock-induced separation upstream of the geometric discontinuity in the ramp. In figure 28(c), the oblique shock system internal to the plume is detected as thin white lines in the focusing schlieren photograph. Flow entrainment of ambient air produced two vortices whose trails appeared along the ramp downstream of the shock line and met near $x/L = 0.65$. The flow patterns observed along the ramp resembled those from wedge nozzles (ref. 30) and other computational investigations of SERN's (refs. 25 to 27 and 29). However, the conditions simulated at NPR = 10 and 13 herein were significantly more overexpanded. The shock location and vortex trails observed in reference 30 along wedge nozzles at overexpanded conditions were similar to those found in the current work because the geometry of the wedge nozzle, with a symmetric upper and lower external expansion ramp, is similar to that of a SERN. As expected, the 3D flow detected along the ramp in this experiment was not modeled with the 2D grid used in the computational study, and as with most computational codes, PAB3D had difficulty predicting solutions that contained such massive areas of unsteady flow separation.

The predicted and experimental normalized static pressure distributions are shown in figure 29 as a function of normalized axial location. A sketch of the nozzle geometry is included to aid the reader in identifying geometric characteristics that impact flow characteristics. The static pressure ratios up through the first discontinuity in the expansion-ramp geometry were accurately predicted. The code predicted the overexpansion and compression at the throat, $x/L = 0.3$, which were not detected in the experimental data because of the limited number of orifices. Large oscillations in predicted static pressure ratios were observed downstream of the shock, along with separated flow over the expansion ramp, for several thousand iterations. An instability appeared to propagate downstream of the separation line with little dampening. Insufficient evidence exists to verify whether this instability was numerical or truly physical. Because no cross-stream component is present in a 2D simulation, the oscillations may have resulted from the lack of 3D relief.

At NPR = 13, the density gradients along the centerline (fig. 28(c)) and the predicted Mach contours up to the shock-induced separation line after 34 054 iterations (fig. 30) were qualitatively similar. At this overexpanded condition, a shock was detected as a line located at $x/L = 0.44$ in the paint-oil flow (fig. 28(b)), as a thin white line in the density gradients along the centerline (fig. 28(c)), and as condensed Mach contours emanating from the discontinuity near $x/L = 0.46$ (fig. 30). The dashed line that extends from the cowl to the upper ramp in figure 30 represents the sidewall (which hides a portion of the flow in fig. 28(c)). The expansion wave from the upper ramp discontinuity at $x/L = 0.306$, the reflection on the free boundary, and the oblique shock system were detected in both figures 28(c) and 30.

Computational Results at NPR = 102

The concave ramp, high Mach number nozzle was also simulated at the design point NPR_D of 102. The predicted axial thrust ratio F_A/F_i was 0.886 and the resultant thrust ratio F_r/F_i was 0.906. The predicted resultant pitch thrust-vector angle of $\delta_p = 12.08°$ corresponded to the 2-percent difference between the axial and resultant thrust ratios. The predicted discharge coefficient was $C_d = 0.939$.

The solution performance convergence history at NPR = 102 is shown in figure 31. The on-design computation converged to a stable solution after only 3000 iterations compared with the far off-design computation at NPR = 13 (fig. 27), which was not converged after 34 054 iterations. The predicted Mach contours at NPR = 102 are shown in figure 32. The high-pressure air expanded approximately 60° around the trailing edge of the cowl as a result of the underexpanded conditions ($p > p_a$) at the cowl exit. Waves from the overexpansion and compression at the throat discontinuity and from the discontinuity in the expansion-ramp geometry were predicted. The shear layer was evident as a dense region of Mach contours. An oblique shock originating near the trailing edge of the ramp is predicted inside the shear layer, detected by more tightly packed Mach contours. The lack of separation along the expansion ramp resulted in quick

convergence of a stable solution with negligible variance of the performance parameters.

The predicted normalized static pressure distribution at each grid density level, as a function of nondimensional axial location, is shown in figure 33. A sketch of the nozzle geometry is included in figure 33 to aid the reader in identifying geometric characteristics that impact flow characteristics. The typical overexpansion and compression of the flow at the throat was predicted near $x/L = 0.31$. The pressure ratio distribution along the expansion ramp indicates that the nozzle was not operating as expected at the design condition because the pressure along the divergent section did not continually expand to the ambient pressure. For the design NPR of 102, the flow would be expected to expand to a pressure ratio of 0.0098 and a Mach number of 3.7 at the ramp trailing edge. The flow was predicted to expand beyond ambient conditions downstream of the discontinuity in the ramp surface geometry at $x/L = 0.46$ and then recompress near $x/L = 0.91$. An oblique shock was predicted in the Mach contours near the trailing edge of the ramp (fig. 32). One might conclude that the nozzle was still overexpanded at this condition and that the theoretical $NPR_D = 102$ is not correct. However, the large positive resultant pitch thrust-vector angle, the somewhat lower axial thrust ratio, and the predicted shape of the plume are usually associated with an underexpanded nozzle. Therefore, the shock at the end of the expansion ramp would have resulted from the slight change in geometric slope of the ramp, from 10.96° to 7.58° near $x/L = 0.91$. The compression of supersonic flow from this geometric reflex would result in an oblique shock. The predicted pressure ratio upstream of the shock at $x/L = 0.91$ corresponded to $M \approx 4.4$. The Mach number downstream of the shock was estimated to be ≈4, and the shock wave angle was estimated to be approximately 15.5° for a deflection angle of 3.38°. The predicted pressure ratio at the trailing edge of the ramp corresponded to $M \approx 3.8$.

The grid sensitivity study for the design case, $NPR_D = 102$, is shown in figures 33 and 34. Grid refinement caused minimal variations in normalized static pressure distributions along the expansion ramp (fig. 33). Axial thrust ratio changed 0.3 percent from the coarse to medium mesh refinement and a mere 0.04 percent at the fine mesh refinement (fig. 34). At the medium and fine mesh refinements, the resultant pitch thrust-vector angle changed 3.8 and 0.77 percent and discharge coefficient changed 0.2 and 0.01 percent, respectively. The minor changes in internal nozzle performance at the fine mesh refinement indicate minimal dependency of the solution on grid mesh density.

Concluding Remarks

The objective of this study was to analyze a nozzle concept, intended to improve the off-design performance of a single-expansion-ramp nozzle (SERN), at low nozzle pressure ratios (NPR's). The capability of translating the throat of the nozzle provides the SERN with a variable expansion ratio to maximize internal nozzle performance over a wide range of flight conditions. Three throat locations were investigated to simulate the application at subsonic-transonic (low Mach number nozzle), low supersonic (intermediate Mach number nozzle), and high supersonic (high Mach number nozzle) flight conditions. Two expansion-ramp surfaces, one concave and one convex, were investigated for each throat location at nozzle pressure ratios up to 13. The low Mach number nozzle was tested at typical operating conditions, whereas the intermediate and high Mach number nozzles were highly overexpanded at all test conditions. The Reynolds averaged Navier-Stokes code PAB3D with a k-ε turbulence model was used to simulate the concave ramp, low Mach number nozzle at NPR's of 5, 9, and 13 and to simulate the concave ramp, high Mach number nozzle at NPR's of 10, 13, and 102.

The experimental results indicate that the concave ramp, low Mach number nozzle had the highest axial thrust ratio over the test NPR range. This result is important because it supports the concept of translating the throat of a SERN from a large expansion ratio to a small expansion ratio in order to provide a more optimum expansion at low operating conditions. Computational solutions verified the axial thrust ratio performance with predicted values within 1.5 percent of experimental data. Additionally, a small value of resultant pitch thrust-vector angle was obtained at the design point ($NPR_D = 9$) of the concave ramp, low Mach number nozzle from both the experimental and computational investigations. Translating the throat from a high to a low expansion ratio provided a decrease in vector angle of 7° at NPR = 9. This result is important because less trim control would be

required at NPR = 9. In general, the nozzles with the concave ramp surface outperformed their convex ramp surface counterparts. The convex ramp surface with a positive initial expansion angle at the throat hindered the expansion of the plume along the expansion ramp and increased the resultant pitch thrust-vector angle.

The quantitative and qualitative comparisons between predicted and experimental data were generally very good. The plume shear layer, oblique shock system, and separation from the external expansion ramp were observed in both the density gradients along the nozzle centerline and in the predicted Mach contours. The flow remained essentially two-dimensional up to the shock-induced separation line. The flow pattern downstream of the shock was representative of a complex, three-dimensional plume. The entrainment of ambient air created vortical flow in the separated, low-pressure region along the expansion ramp. A two-dimensional computational domain provided good prediction of performance quantities and of flow characteristics near on-design conditions where minimal separation occurred along the ramp. As a result of a numerical or physical instability, converged solutions at far off-design conditions (NPR = 10 and 13) were not obtained for the high Mach number nozzle. However, good qualitative comparisons were obtained up to the shock-induced separation line.

Future high-speed aircraft will require high overall performance throughout a range of flight conditions. The initial experimental and computational results of the translating-throat SERN concept indicated some promising performance benefits. Furthermore, a SERN with a variable expansion ratio would provide additional performance benefits of a SERN over other nozzle candidates, such as ease of integration with the airframe, potential weight reductions, and potential drag reductions.

Appendix

Uncertainty Analysis

An uncertainty analysis was conducted to determine the estimated uncertainty associated with axial thrust ratio, discharge coefficient, and resultant pitch thrust-vector angle for the comparison between computational predicted values and experimental data. (See figs. 20 and 21.) This uncertainty analysis was implemented in a spreadsheet form for many of the flow measurements and data reduction equations used in the Langley Jet Exit Test Facility. A full description of the uncertainty analysis is given in reference 17. To determine the propagation of error of individual measurements in a data reduction equation,

$$r = r(x_1, x_2, \ldots, x_J) \tag{A1}$$

the following uncertainty analysis expression was utilized:

$$B_r = \left[\left(\frac{\partial r}{\partial x_1}B_1\right)^2 + \left(\frac{\partial r}{\partial x_2}B_2\right)^2 + \ldots + \left(\frac{\partial r}{\partial x_J}B_J\right)^2\right]^{1/2} \tag{A2}$$

The quantity $\frac{\partial r}{\partial x_1}B_1$ represents the uncertainty contribution of the measurement x_1 to the data reduction equation r. Each contribution is combined in a root sum square to estimate the total uncertainty of the data reduction equation. This analysis was conducted for the low and high Mach number nozzles with the concave expansion ramp; the estimated uncertainties are included in tables 4 and 5. The spreadsheet was utilized to estimate the uncertainties of NPR, C_d, F_A/F_i, F_r/F_i, and δ_p and required the following inputs:

1. The operating conditions: NPR, p_a, $T_{t,j}$, and A_t

2. The system setup, including the number of jet total pressure measurements, the number of thermocouples, the number of venturi static pressure measurements, and the curve fit used for weight flow

3. The individual instrument uncertainty as a percent of reading for $T_{t,j}$, $p_{t,j}$, p_a, normal force 2σ, and axial force 2σ

References

1. Treager, Irwin E.: *Aircraft Gas Turbine Engine Technology*, Third ed. McGraw-Hill, 1996.
2. Capone, F. J.: The Nonaxisymmetric Nozzle—It Is for Real. AIAA-79-1810, Aug. 1979.
3. Johnson, Donald B.; Espinosa, Angel M.; and Althuis, Jeffrey S.: NASP Derived Vehicles—Not Just to Space. AIAA-92-5020, Dec. 1992.
4. Dusa, D. J.: High Mach Propulsion System Installation and Exhaust System Design Considerations. AIAA-87-2941, Sept. 1987.
5. Kuchar, A. P.; and Wolf, J. P.: Preliminary Assessment of Exhaust Systems for High Mach (4 to 6) Fighter Aircraft. AIAA-89-2356, July 1989.
6. Dusa, D. J.: Turboramjet Exhaust Nozzle Systems. *Tenth International Symposium on Air Breathing Engines*, X ISABE, Sept. 1991, pp. 1–11.
7. Carboni, Jeanne D.; Shyne, Rickey J.; Leavitt, Laurence D.; Taylor, John G.; and Lamb, Milton: *Supersonic Investigation of Two Dimensional Hypersonic Exhaust Nozzles*. NASA TM-105687, 1992.
8. Capone, Francis J.; Re, Richard J.; and Bare, E. Ann: *Parametric Investigation of Single-Expansion-Ramp Nozzles at Mach Numbers From 0.60 to 1.20*. NASA TP-3240, 1992.
9. Re, Richard J.: *Static Internal Performance of Single-Expansion-Ramp Nozzles With Various Combinations of Internal Geometric Parameters*. NASA TM-86270, 1984.
10. Bare, E. Ann; and Capone, Francis J.: *Static Internal Performance of Convergent Single-Expansion-Ramp Nozzles With Various Combinations of Internal Geometric Parameters*. NASA TM-4112, 1989.
11. Berrier, B. L.; and Leavitt, L. D.: *Static Internal Performance of Single-Expansion-Ramp Nozzles With Thrust-Vectoring Capability up to 60°*. NASA TP-2364, 1984.
12. Berrier, Bobby L.; Leavitt, Laurence D.; and Bangert, Linda S.: *Operating Characteristics of the Multiple Critical Venturi System and Secondary Calibration Nozzles Used for Weight-Flow Measurements in the Langley 16-Foot Transonic Tunnel*. NASA TM-86405, 1985.
13. Weinstein, Leonard M.: An Improved Large-Field Focusing Schlieren System. AIAA-91-0567, Jan. 1991.
14. Mercer, Charles E.; Berrier, Bobby L.; Capone, Francis J.; and Grayston, Alan M.: *Data Reduction Formulas for the 16-Foot Transonic Tunnel—NASA Langley Research Center, Revision 2*. NASA TM-107646, 1992.
15. Hunter, Craig Allen: An Experimental Analysis of Passive Shock-Boundary Layer Interaction Control for Improving the Off-Design Performance of Jet Exhaust Nozzles. M.S. Thesis, The George Washington Univ., Sept. 1993.
16. *A User's Guide to the Langley 16-Foot Transonic Tunnel Complex—Revision 1*. NASA TM-102750, 1990. (Supersedes NASA TM-83186.)
17. Coleman, Hugh W.; and Steele, W. Glenn, Jr.: *Experimentation and Uncertainty Analysis for Engineers*. John Wiley and Sons, 1989.
18. Abdol-Hamid, Khaled S.: Application of a Multiblock/Multizone Code (PAB3D) for the Three-Dimensional Navier-Stokes Equations. AIAA-91-2155, June 1991.
19. Abdol-Hamid, Khaled S.; Lakshmanan, B.; and Carlson, John R.: *Application of Navier-Stokes Code PAB3D With k-ε Turbulence Model to Attached and Separated Flows*. NASA TP-3480, 1995.
20. Van Leer, Bram: *Flux-Vector Splitting for the Euler Equations*. ICASE Rep. No. 82-30, 1982.
21. Roe, P. L.: Characteristic-Based Schemes for the Euler Equations. *Ann. Rev. Fluid Mech.*, vol. 18, 1986, pp. 337–365.
22. Jones, W. P.; and Launder, B. E.: The Prediction of Laminarization With a Two-Equation Model of Turbulence. *Int. J. Heat & Mass Trans.*, vol. 15, Feb. 1972, pp. 301–314.
23. Carlson, John R.: *A Nozzle Internal Performance Prediction Method*. NASA TP-3221, 1992.
24. Ames Research Staff: *Equations, Tables, and Charts for Compressible Flow*. NACA Rep. 1135, 1953. (Supersedes NACA TN 1428.)
25. Ruffin, Stephen M.; Venkatapathy, Ethira J.; Lee, Seung-Ho; Keener, Earl R.; and Spaid, Frank, W.: Single Expansion Ramp Nozzle Simulations. AIAA-92-0387, Jan. 1992.
26. Ishiguro, T.; Takaki, R.; Mitani, T.; and Hiraiwa, T.: Three-Dimensional Analysis of Scramjet Nozzle Flows. AIAA-93-5059, 1993.
27. Pierce, M. A.; and Ely, W. L.: A Computational Exploration of the Importance of Three-Dimensionality, Boundary Layer Development, and Flow Chemistry to the Prediction of Scramjet Nozzle Performance. AIAA-91-5059, Dec. 1991.
28. Spaid, Frank W.; and Keener, Earl R.: Experimental Results for a Hypersonic Nozzle/Afterbody Flow Field. AIAA-92-3915, July 1992.
29. Carson, G. T.: *Experimental and Analytical Investigation of a Nonaxisymmetric Wedge Nozzle at Static Conditions*. NASA TP-1188, 1978.
30. Carlson, John R.; and Abdol-Hamid, Khaled S.: Prediction of Static Performance for Single Expansion Ramp Nozzles. AIAA-93-2571, June 1993.

Table 1. Nozzle Configuration Parameters

Nozzle	x_t, in.	l_c, in.	l_r, in.	h_t, in.	h_e, in.	θ_r, deg	ϕ_r, deg	$(A_e/A_t)_{int}$	$NPR_{D,int}$	$(A_e/A_t)_{ext}$	NPR_D
Concave high Mach number	5.17	5.3	11.6	0.400	3.30	−13.9	−14.3	1.08	2.92	8.25	102.4
Convex high Mach number	5.30	5.3	11.6	0.384	3.30	−14.6	1.8	1.00	1.89	8.59	109.1
Concave intermediate Mach number	8.91	9	7.9	0.400	1.85	−10.3	−10.0	1.05	2.60	4.63	42.2
Convex intermediate Mach number	8.91	9	7.9	0.400	1.85	−10.3	−4.8	1.01	2.20	4.63	42.2
Concave low Mach number	12.64	12.7	4.2	0.400	0.73	−4.4	−5.4	1.01	2.23	1.83	9.0
Convex low Mach number	12.70	12.7	4.2	0.385	0.73	−5.9	5.6	1.00	1.89	1.9	9.9

Table 2. Balance Accuracy

Forces and moments	2σ	2σ, percent of balance maximum
Normal	1.52 lb	0.19
Axial	1.64 lb	0.14
Pitch	25.69 in-lb	0.21
Roll	55.60 in-lb	5.56
Yaw	22.44 in-lb	0.19
Side	1.96 lb	0.25

Table 3. Uncertainty Estimates

	Percent of reading
Jet total pressures, $p_{t,j}$	±0.68
Thermocouples, $T_{t,j}$	±0.37
p_a	±0.1
ESP, p	±0.25

Table 4. Uncertainty Estimate for Concave Ramp, Low Mach Number Nozzle

NPR condition	Uncertainty estimate for—				
	NPR	C_d	F_A/F_i	F_r/F_i	δ_p, deg
2.017	0.005	0.003	0.025	0.025	1.058
3.004	0.007	0.003	0.014	0.014	0.573
4.005	0.009	0.003	0.009	0.009	0.379
4.999	0.012	0.003	0.002	0.002	0.284
9.010	0.021	0.003	0.002	0.002	0.140
13.002	0.031	0.003	0.002	0.002	0.008

Table 5. Uncertainty Estimate for Concave Ramp, High Mach Number Nozzle

NPR condition	Uncertainty estimate for—				
	NPR	C_d	F_A/F_i	F_r/F_i	δ_p, deg
2	0.005	0.003	0.025	0.025	1.091
4.004	0.009	0.003	0.009	0.009	0.399
5.027	0.012	0.003	0.007	0.007	0.292
7.011	0.017	0.003	0.005	0.005	0.193
9.001	0.021	0.003	0.004	0.004	0.144
10.006	0.024	0.003	0.004	0.004	0.126
13.007	0.031	0.003	0.003	0.003	0.092

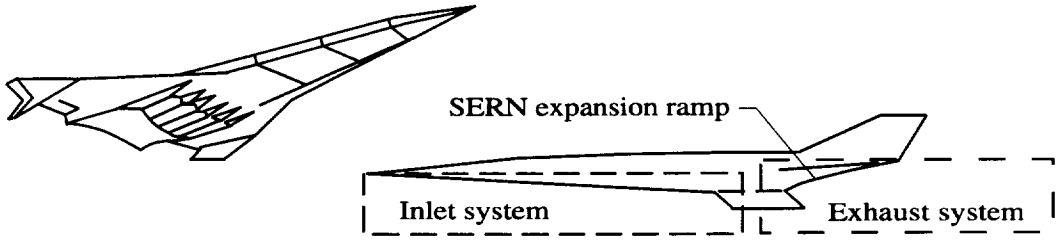

Figure 1. Sketch of highly integrated high-speed vehicle.

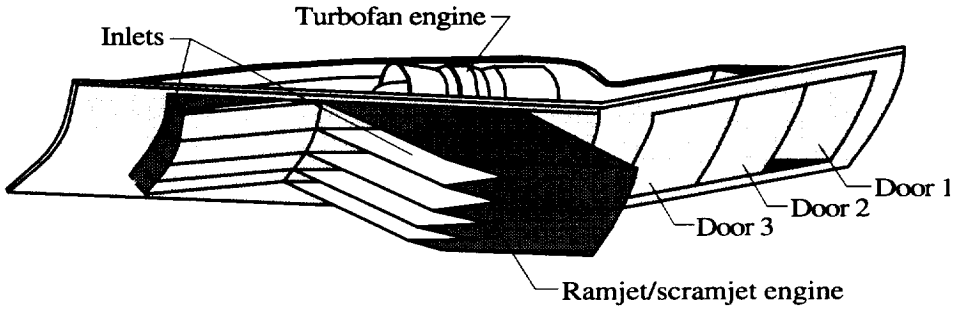

Figure 2. Translating-throat SERN integrated into afterbody of high-speed vehicle.

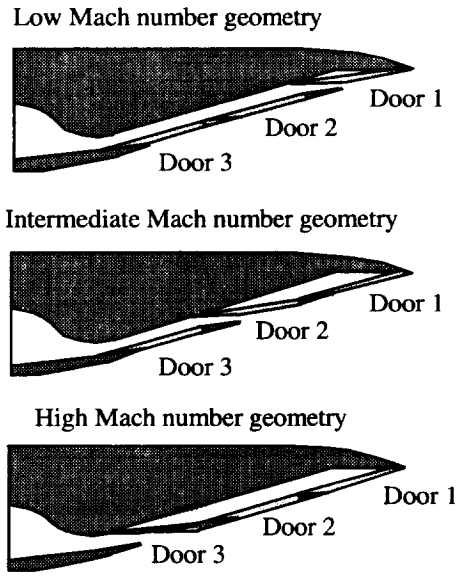

Figure 3. Sketch of translating-throat SERN model.

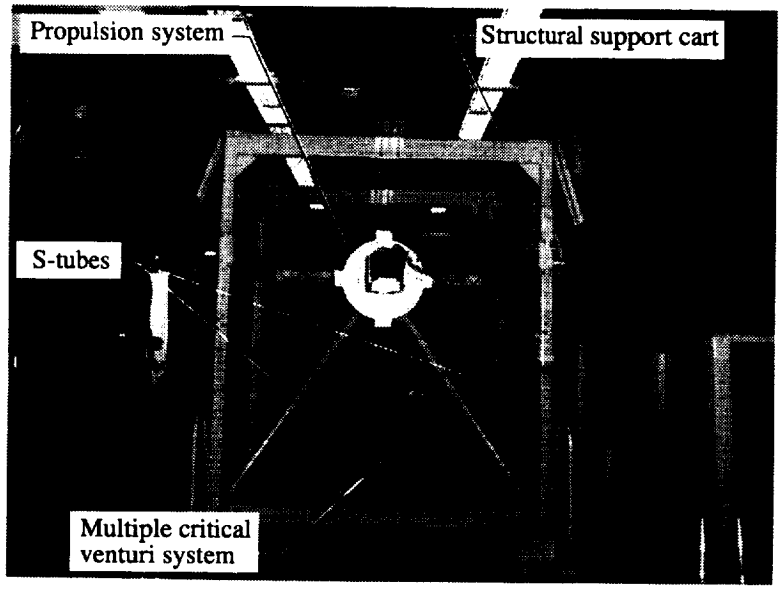

Figure 4. High Mach number nozzle mounted on propulsion system in Langley Jet Exit Test Facility. Looking upstream.

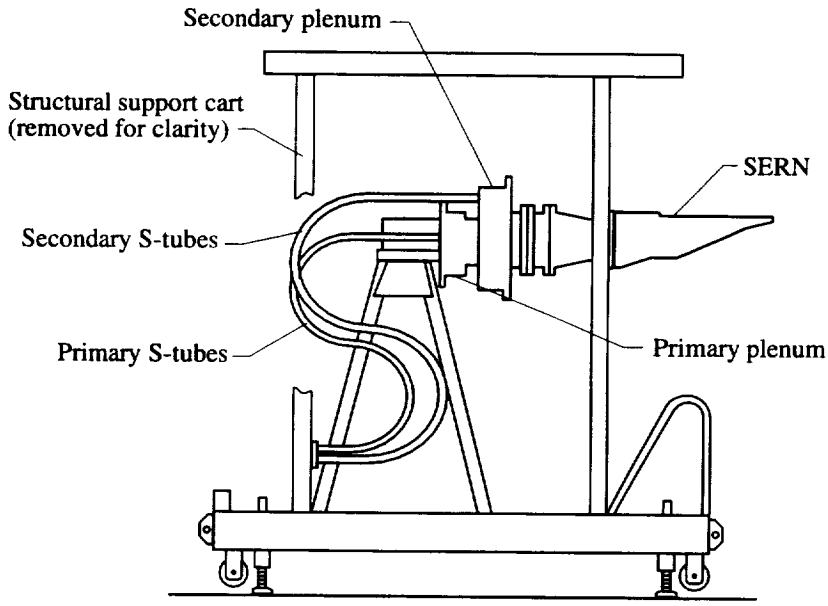

Figure 5. Sketch of propulsion system attached to structural support cart. Side view.

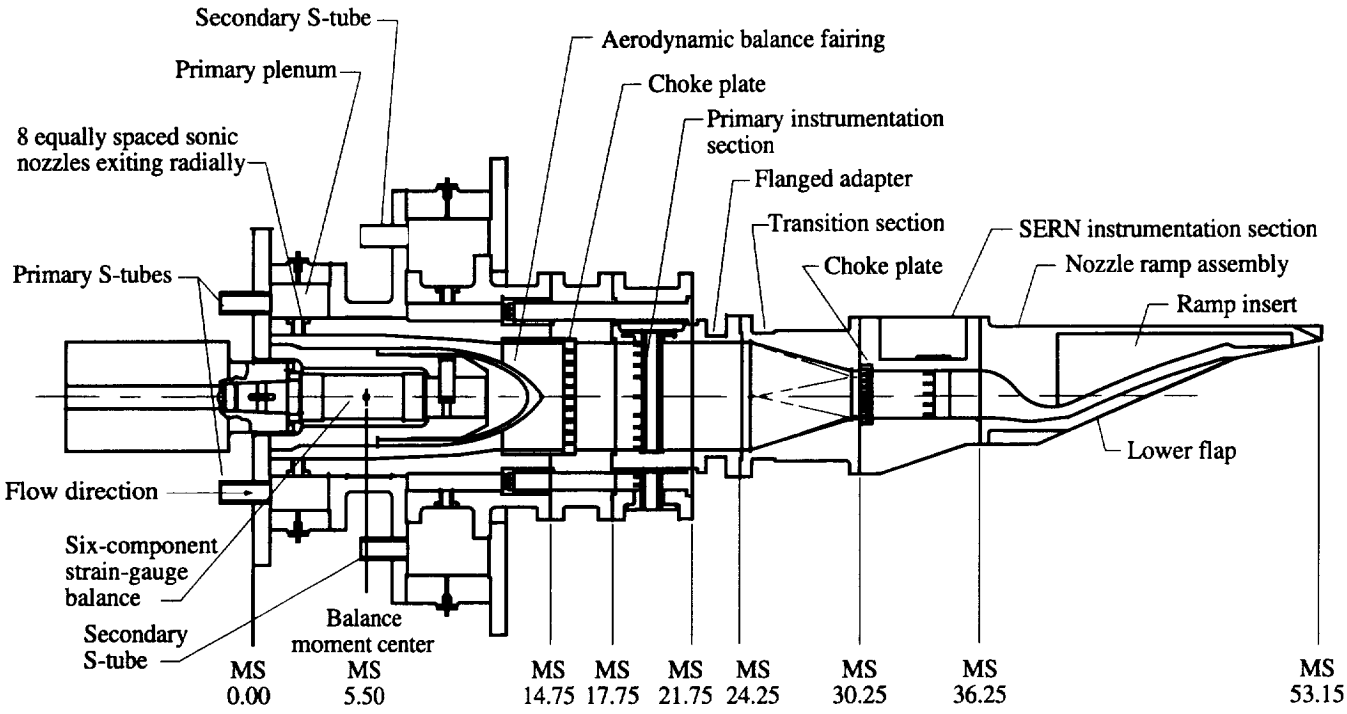

Figure 6. Installation of typical translating-throat SERN nozzle on propulsion simulation system.

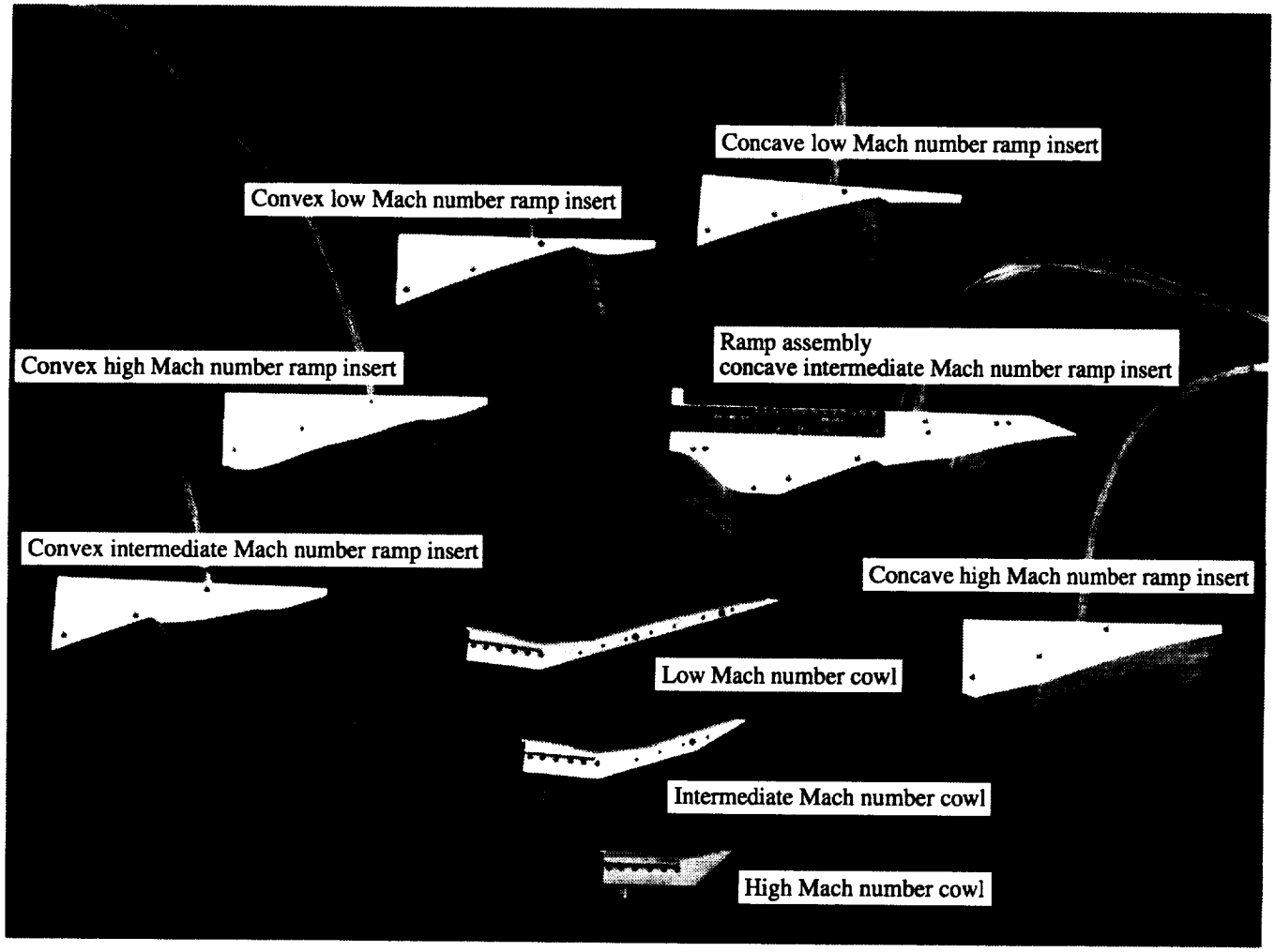

Figure 7. Ramp assembly, six ramp inserts, and three lower cowl pieces (sidewalls not shown).

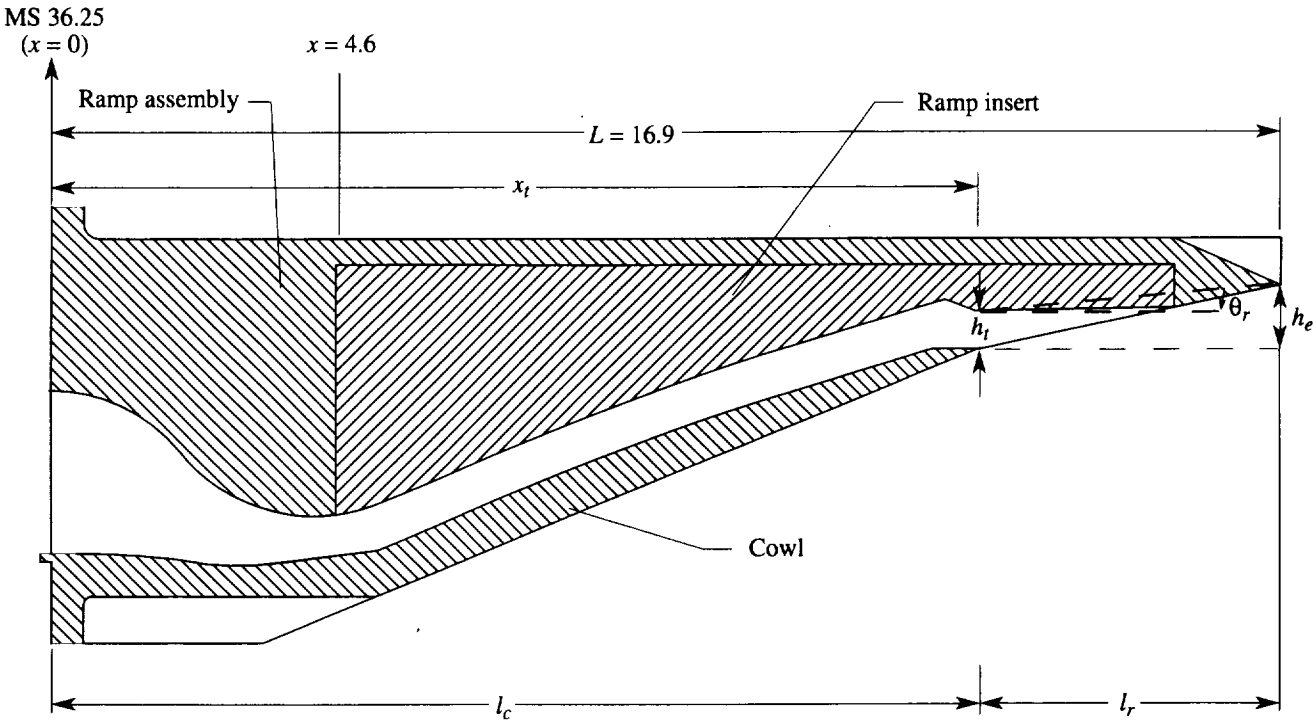

(a) Illustration of geometric parameters.

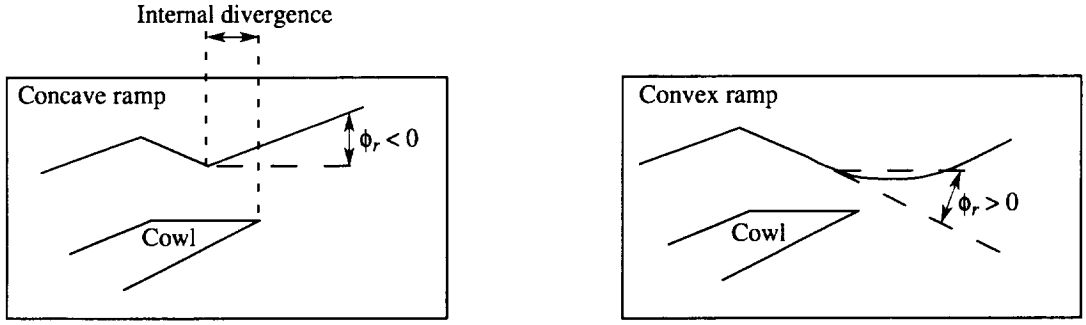

(b) Graphical representation of initial expansion angles at throat.

Figure 8. Description of general single expansion-ramp nozzle. Linear dimensions are in inches; angles are in degrees.

Orifice	x	y	Orifice	x	y
P1	0.95	0.00	P16	15.00	0.00
P2	1.95	0.00	P17	16.50	0.00
P3	2.95	0.00	P18	6.00	1.91
P4	3.94	0.00	P19	7.00	1.91
P5	5.00	0.00	P20	8.00	1.91
P6	6.00	0.00	P21	8.50	1.91
P7	7.00	0.00	P22	9.00	1.91
P8	8.00	0.00	P23	10.00	1.91
P9	8.50	0.00	P24	11.00	1.91
P10	9.00	0.00	P25	12.00	1.91
P11	10.00	0.00	P26	13.00	1.91
P12	11.00	0.00	P27	14.00	1.91
P13	12.00	0.00	P28	15.00	1.91
P14	13.00	0.00	P29	16.50	1.91
P15	14.00	0.00			

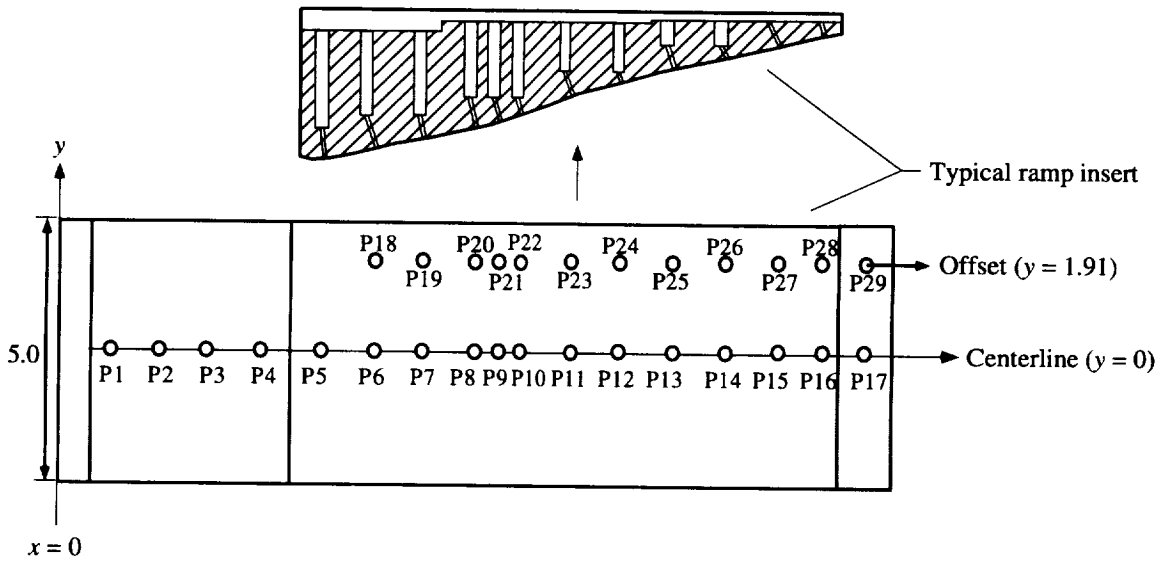

Figure 9. Orientation of static pressure orifices along expansion ramp. Dimensions are in inches.

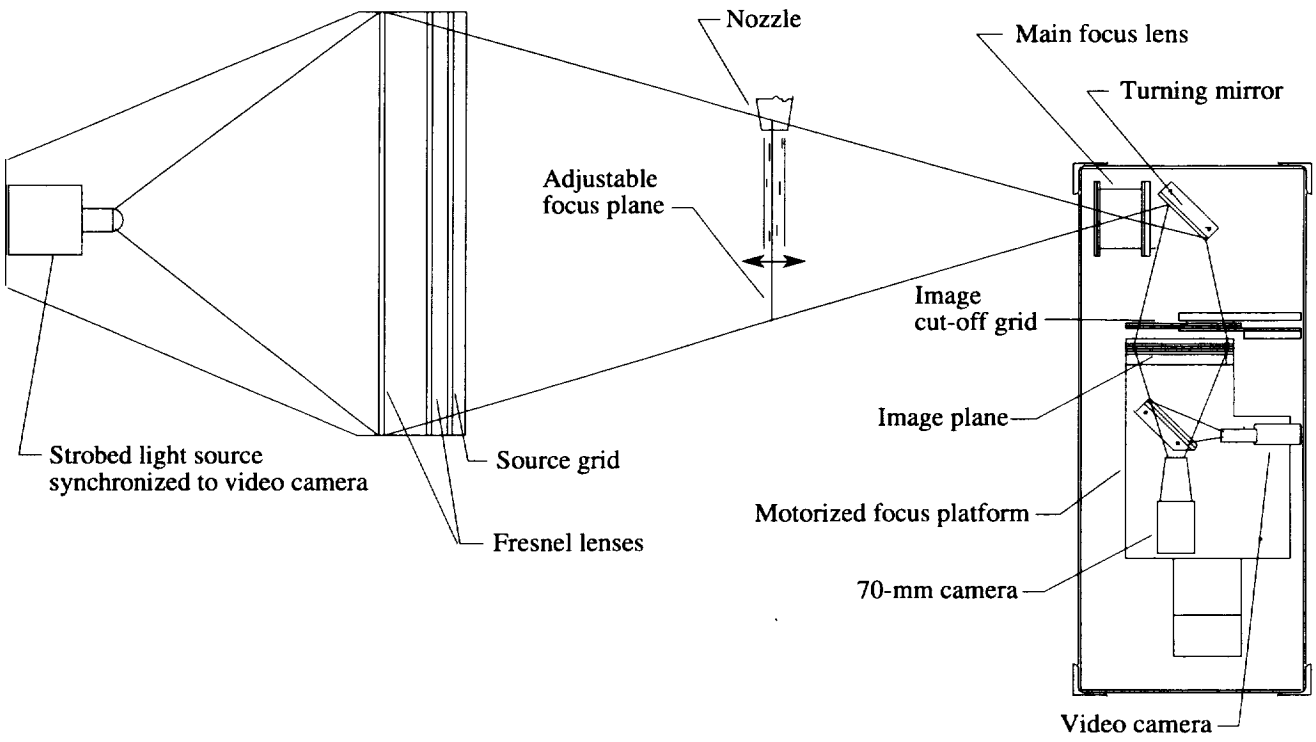

Figure 10. Layout of focusing schlieren flow visualization system.

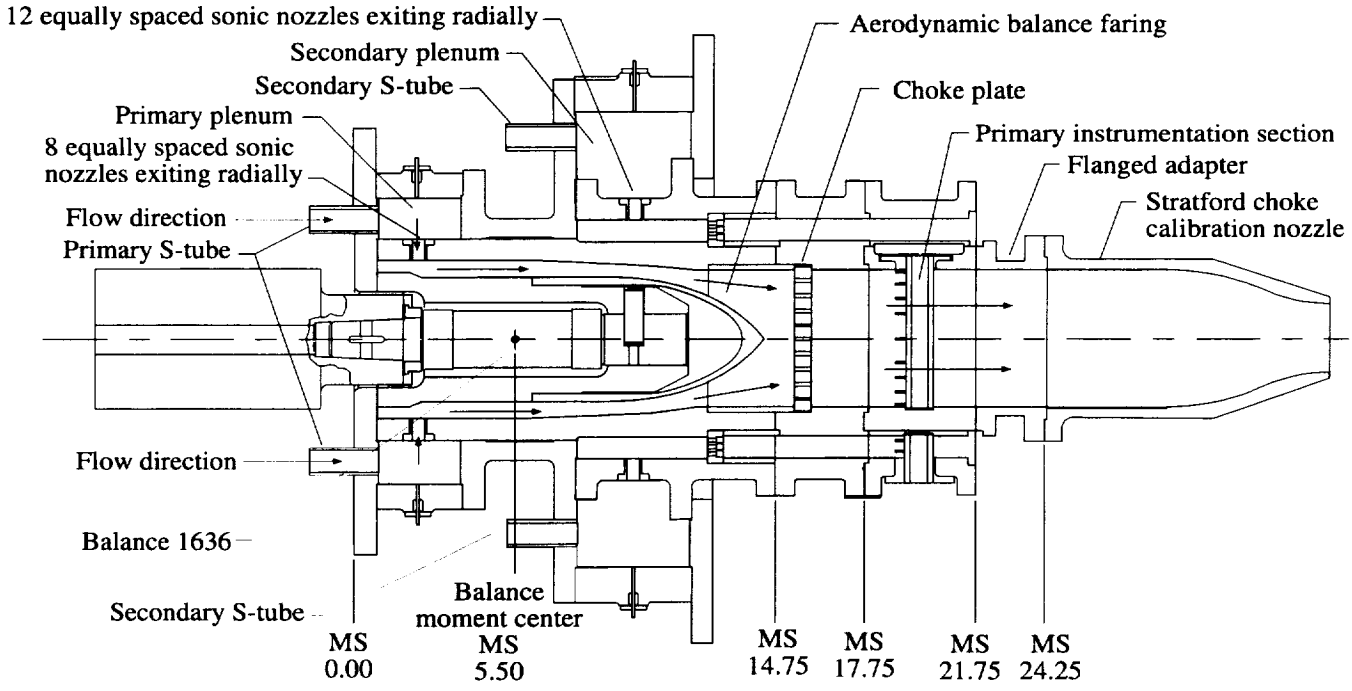

Figure 11. Typical hardware setup for balance calibrations on propulsion simulation system.

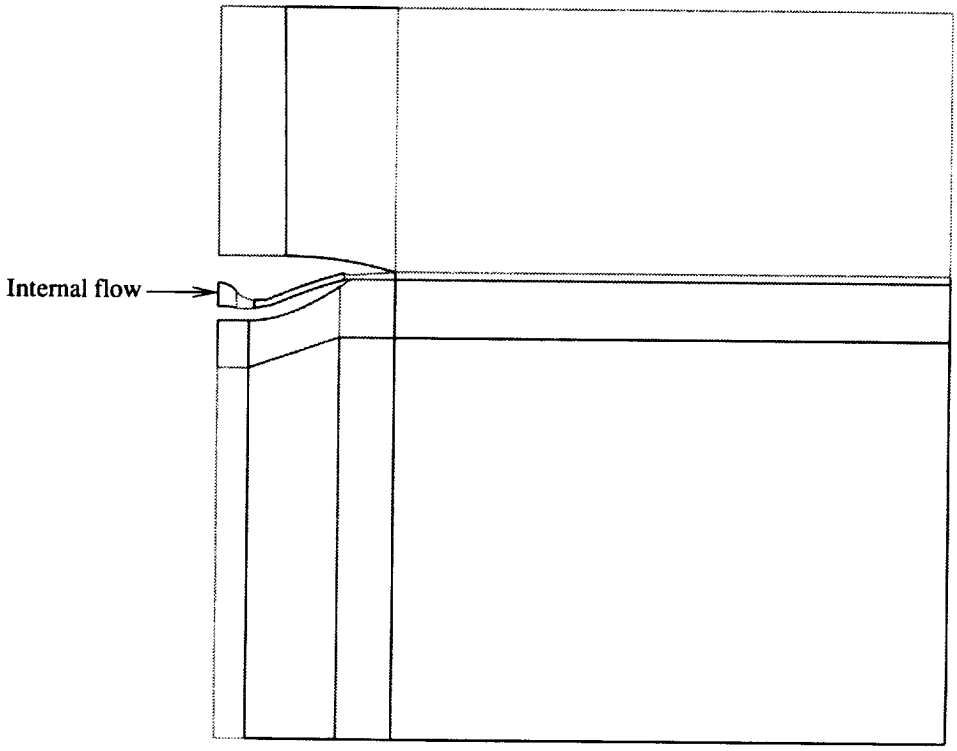

(a) Complete flow field.

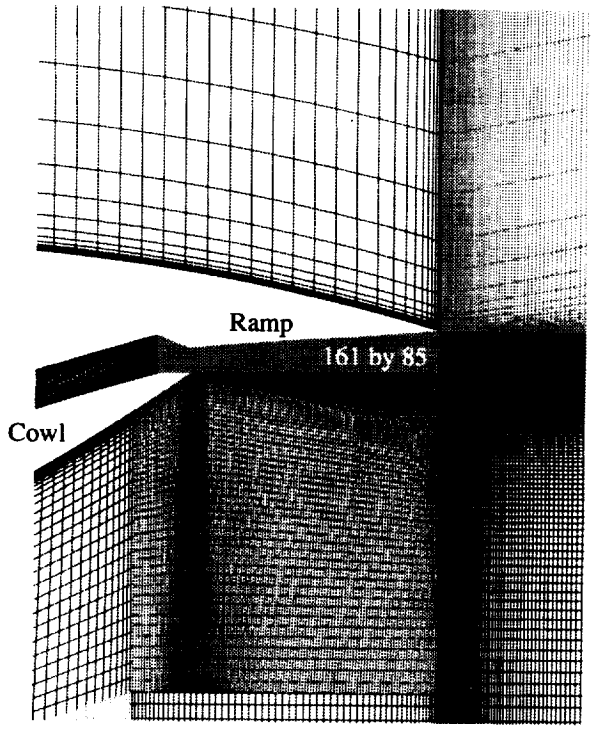

(b) Close-up of throat and ramp.

Figure 12. Computational domain for concave ramp, low Mach number nozzle.

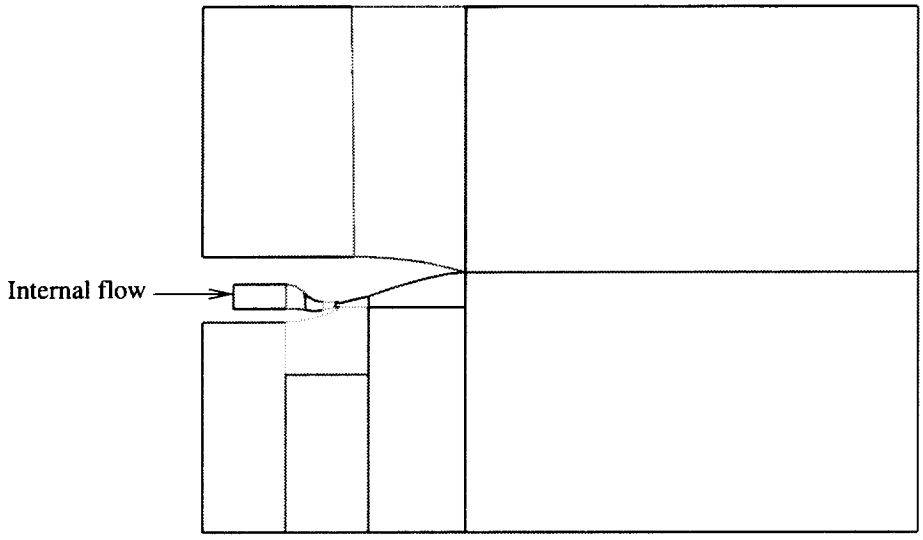

(a) Complete flow field.

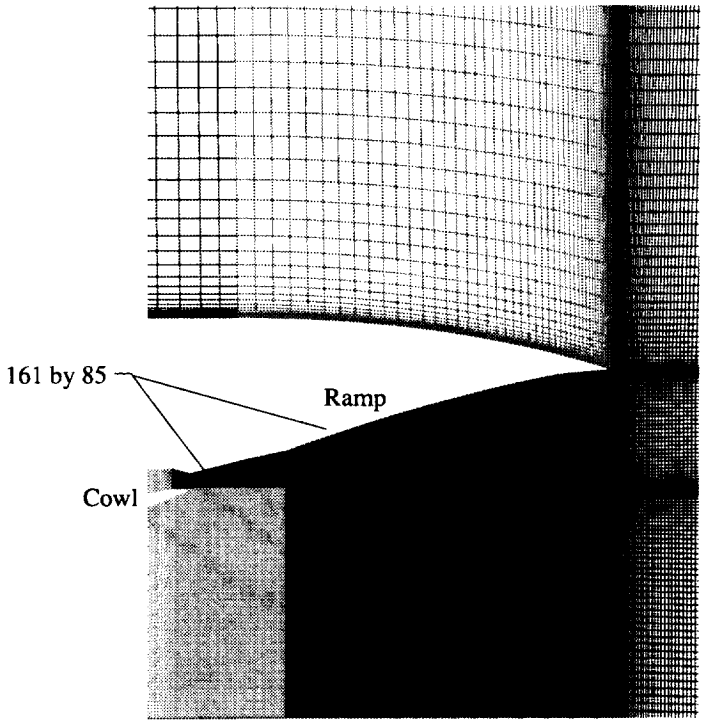

(b) Close-up of throat and ramp.

Figure 13. Computational domain for concave ramp, high Mach number nozzle.

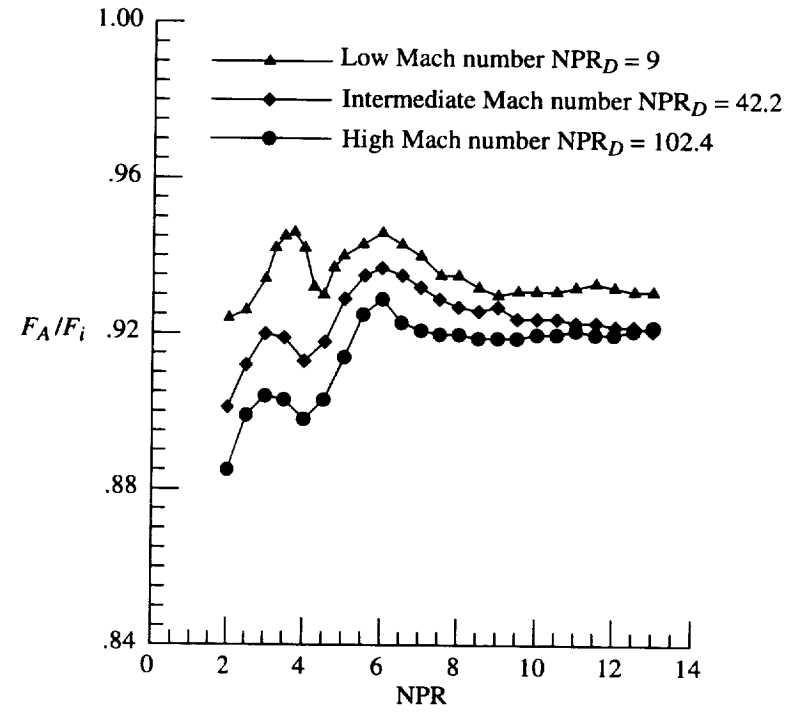

(a) Axial thrust ratio.

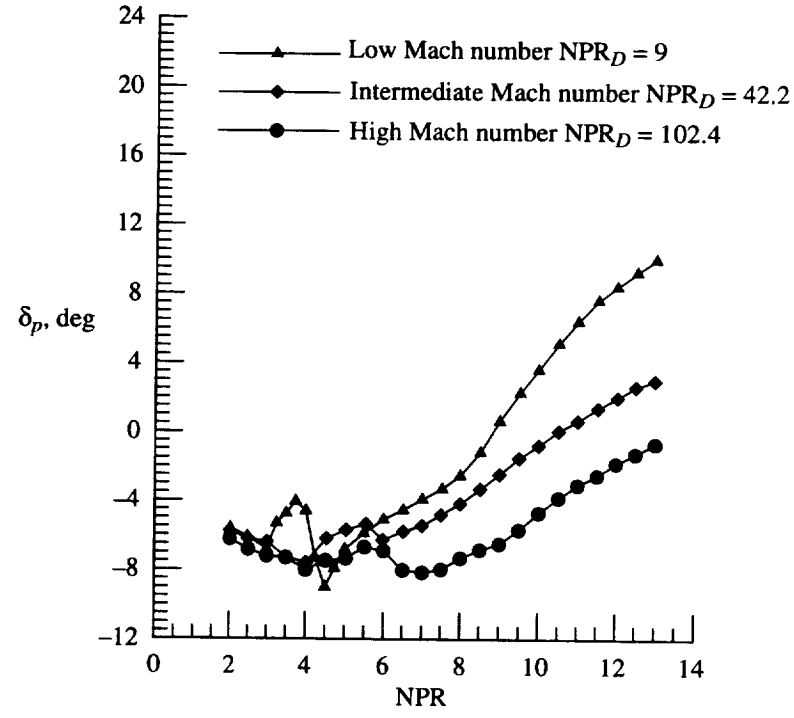

(b) Resultant pitch thrust-vector angle.

Figure 14. Effect of throat location on internal performance of concave ramp nozzles.

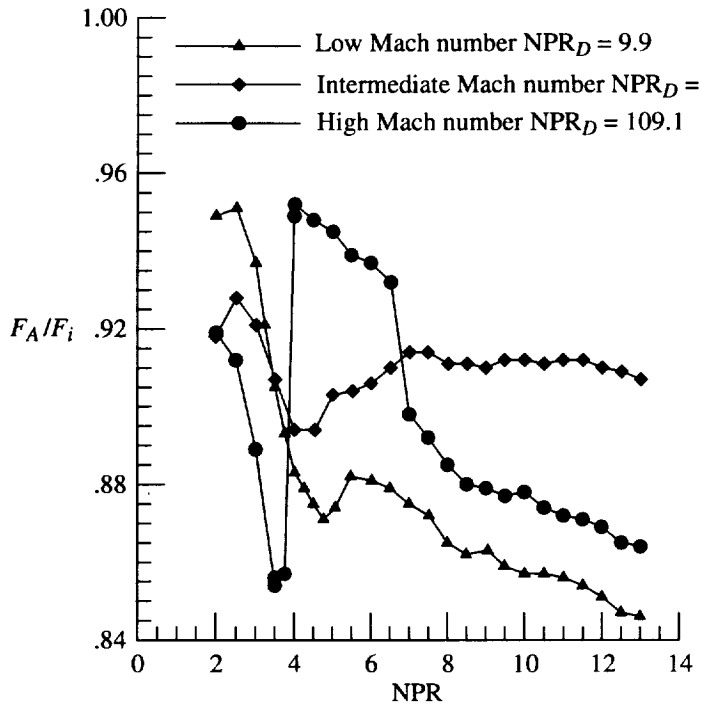

(a) Axial thrust ratio.

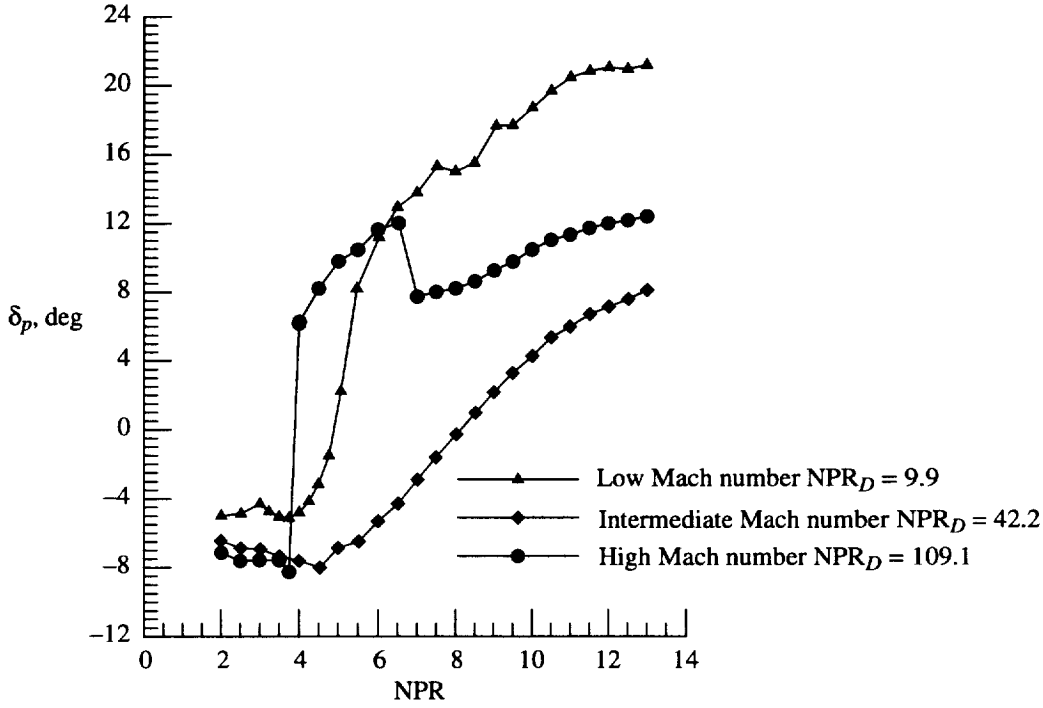

(b) Resultant pitch thrust-vector angle.

Figure 15. Effect of throat location on internal performance of convex ramp nozzles.

(a) Density gradients along nozzle centerline; NPR = 3.75.

(b) Density gradients along nozzle centerline; NPR = 4.

Figure 16. Illustration of separation that occurs along convex expansion ramp, high Mach number nozzle as NPR increases.

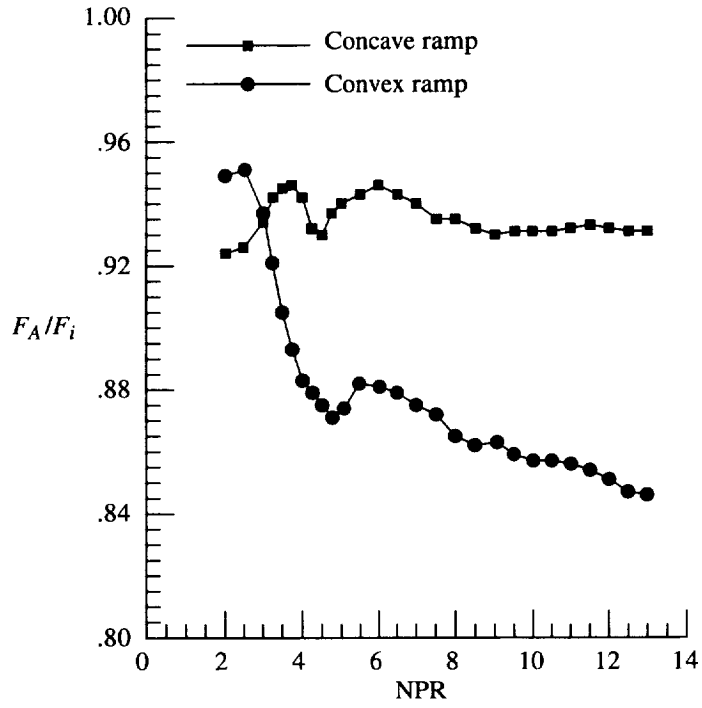

(b) Axial thrust ratio.

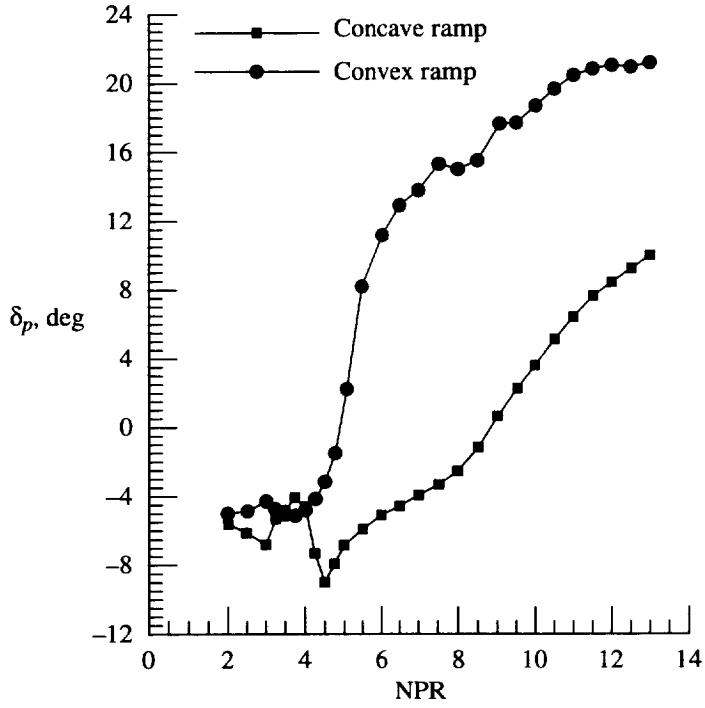

(b) Resultant pitch thrust-vector angle.

Figure 17. Effect of ramp geometry on internal performance of low Mach number nozzles.

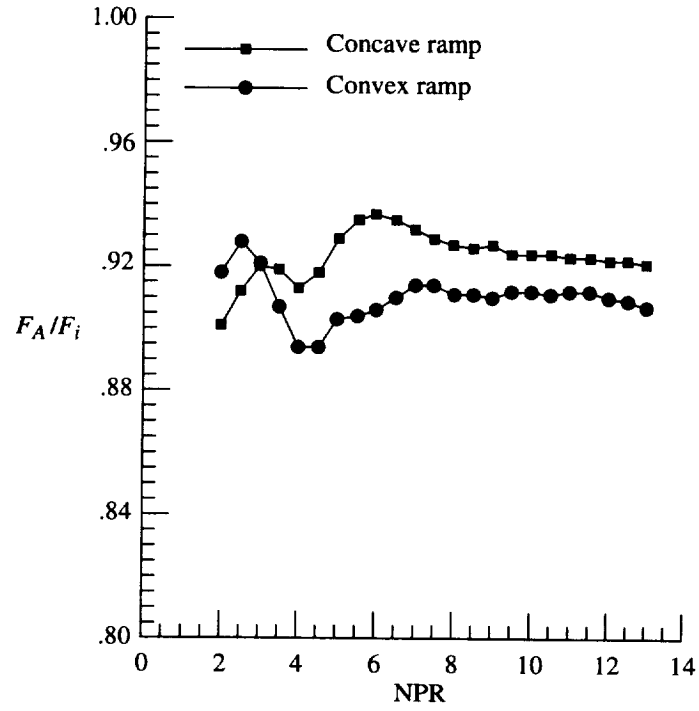

(a) Axial thrust ratio.

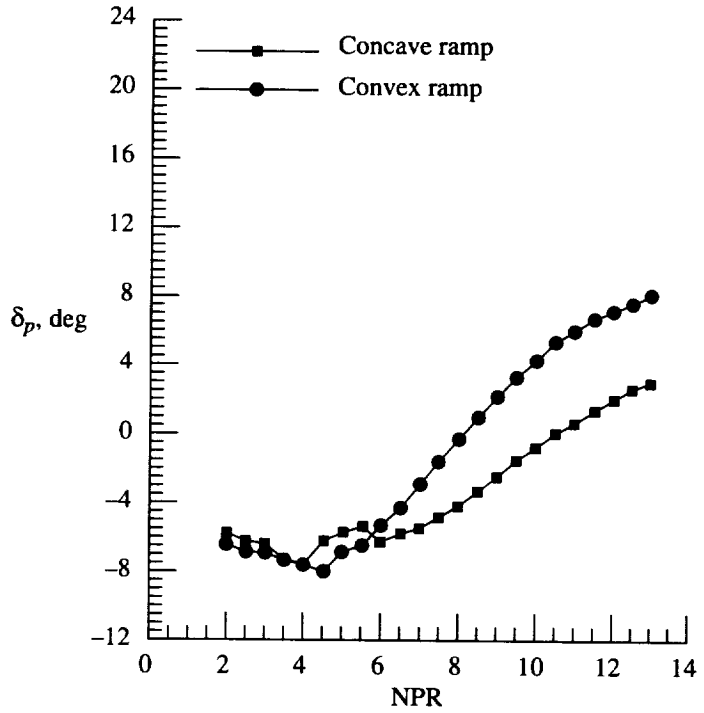

(b) Resultant pitch thrust-vector angle.

Figure 18. Effect of ramp geometry on internal performance of intermediate Mach number nozzles.

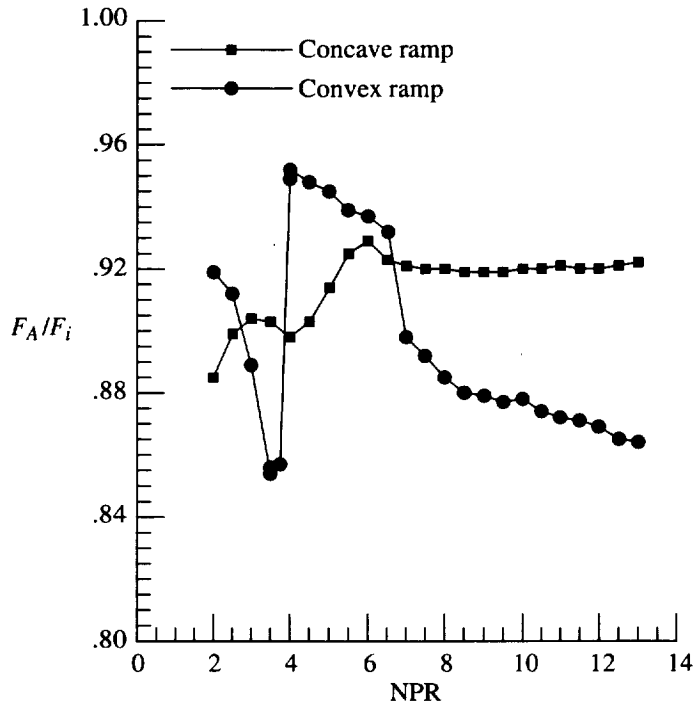

(a) Axial thrust ratio.

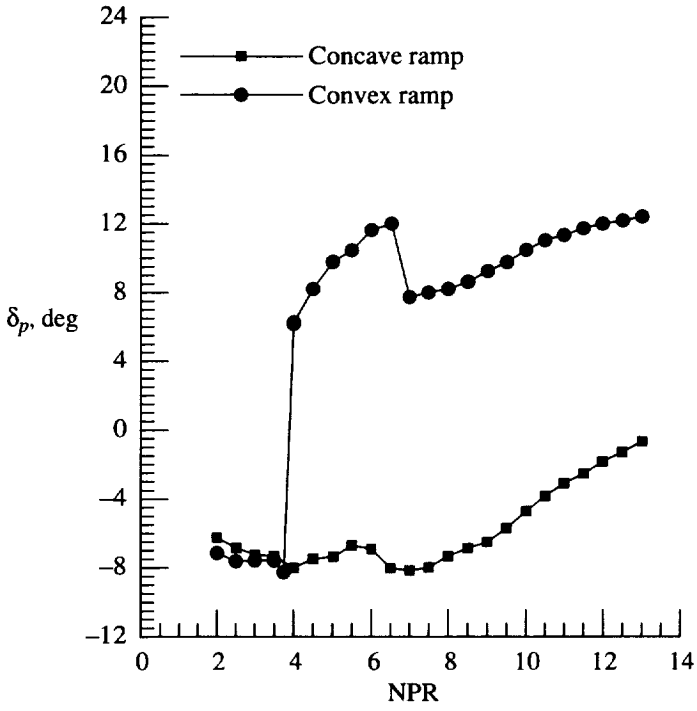

(b) Resultant pitch thrust-vector angle.

Figure 19. Effect of ramp geometry on internal performance of high Mach number nozzles.

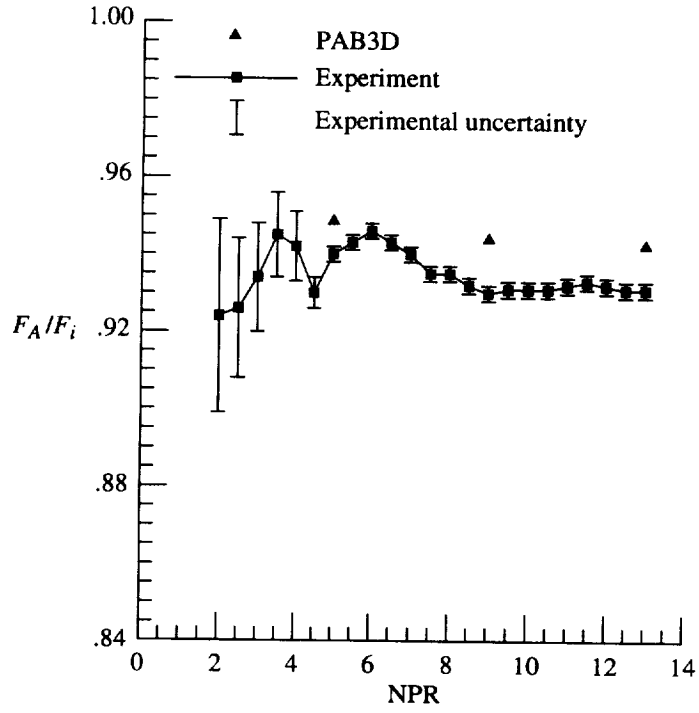

(a) Axial thrust ratio.

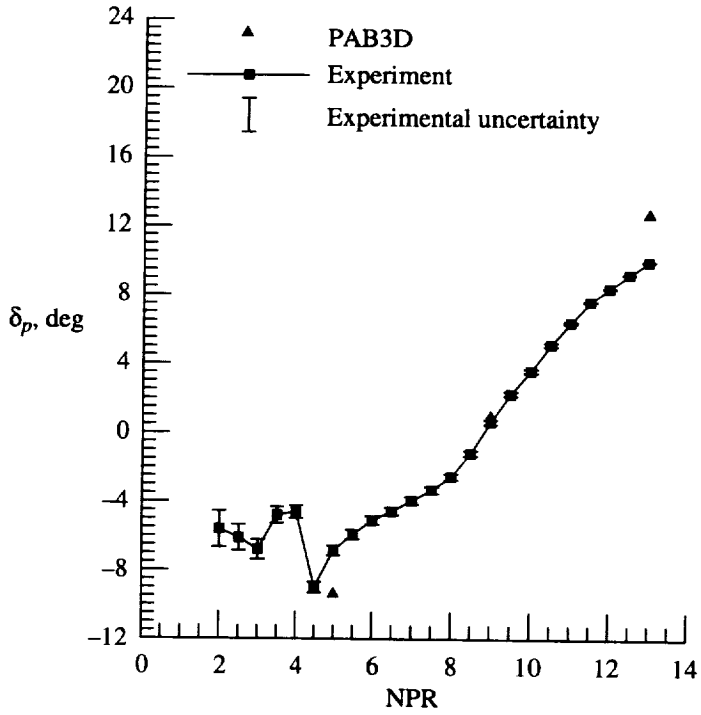

(b) Resultant pitch thrust-vector angle.

Figure 20. Predicted and experimental data for concave ramp, low Mach number nozzle.

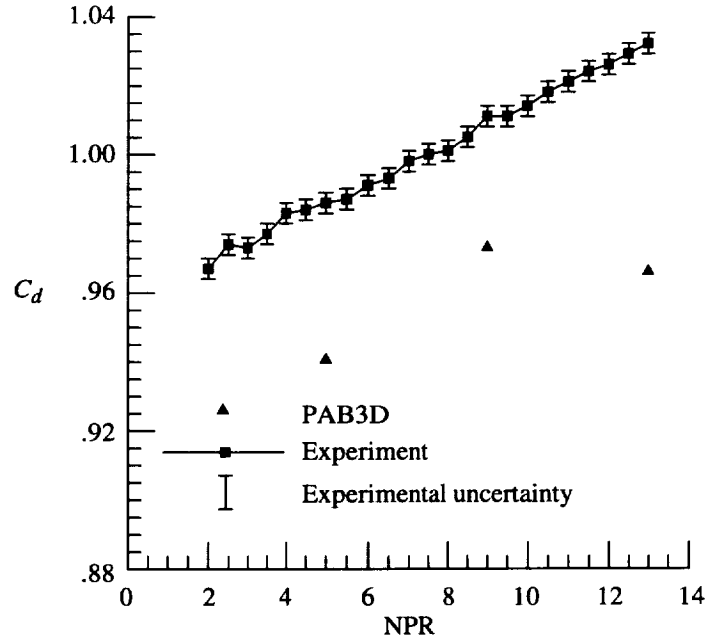

Figure 21. Predicted discharge coefficient and experimental data for concave ramp, low Mach number nozzle.

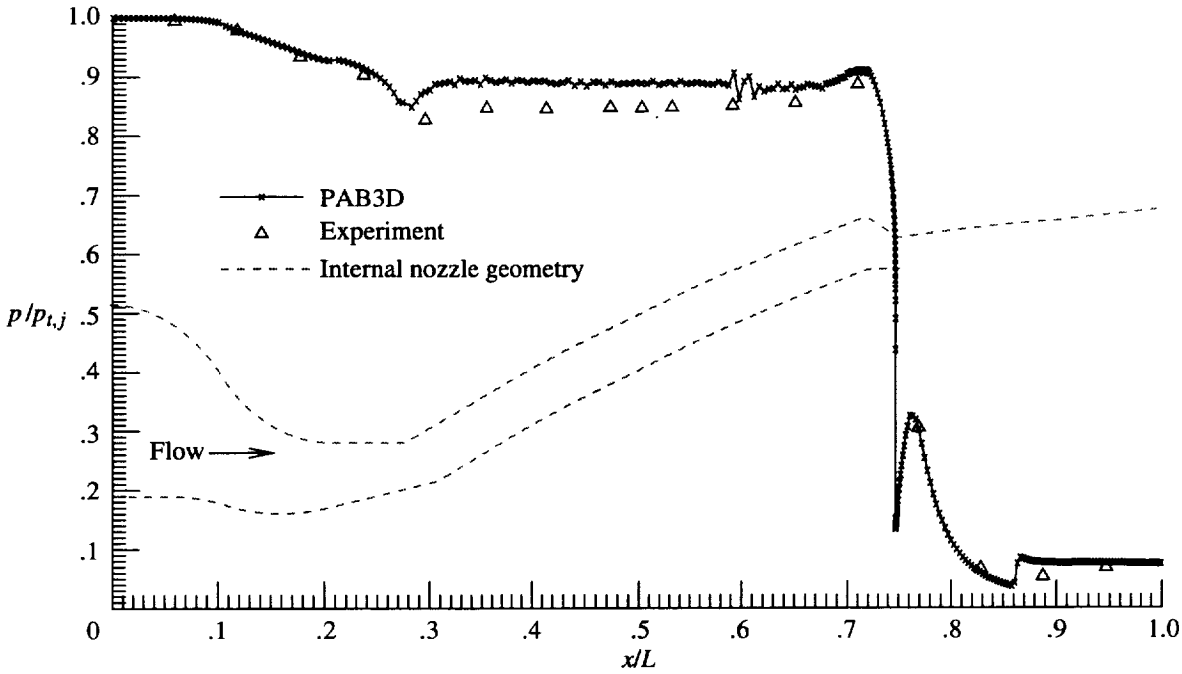

Figure 22. Predicted and experimental normalized static pressure distribution for concave ramp, low Mach number nozzle at $M = 0.05$ and NPR = 13.

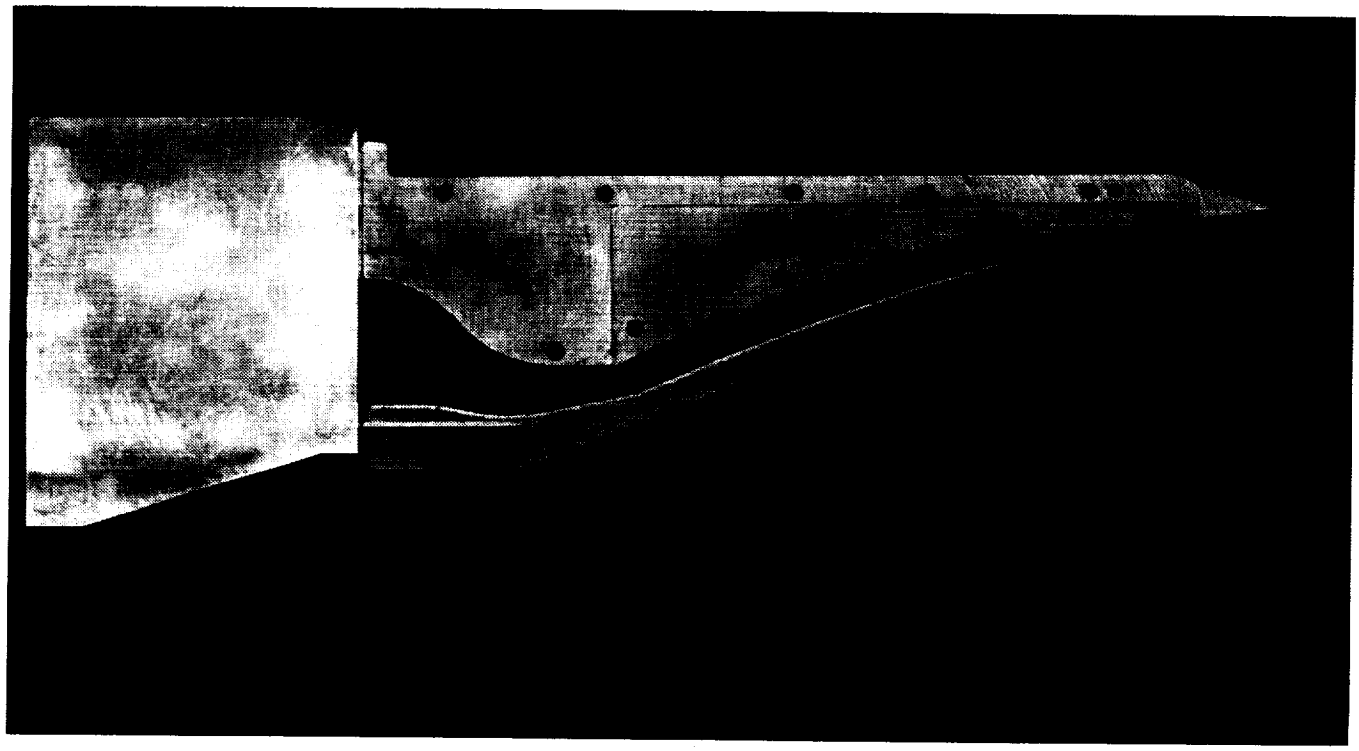

(a) Nozzle configuration with near sidewall removed and mounted to transition section.

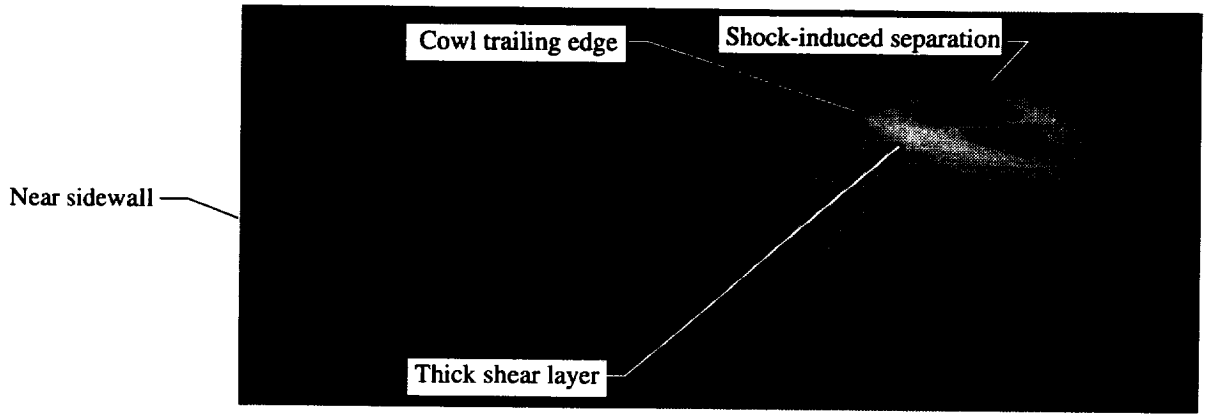

(b) Density gradients along nozzle centerline at NPR = 13.

Figure 23. Concave ramp, low Mach number nozzle.

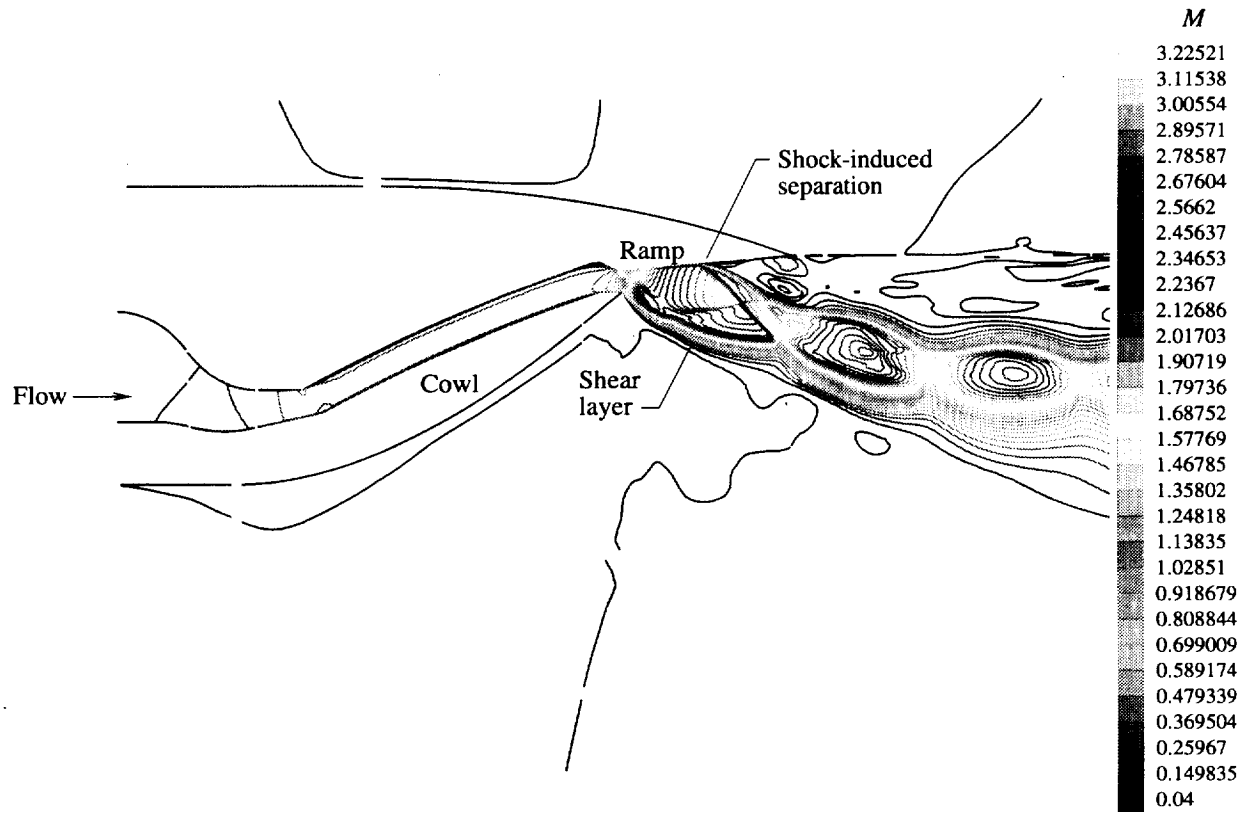

Figure 24. Predicted Mach contours along centerline of concave ramp, low Mach number nozzle at $M = 0.05$ and NPR = 13.

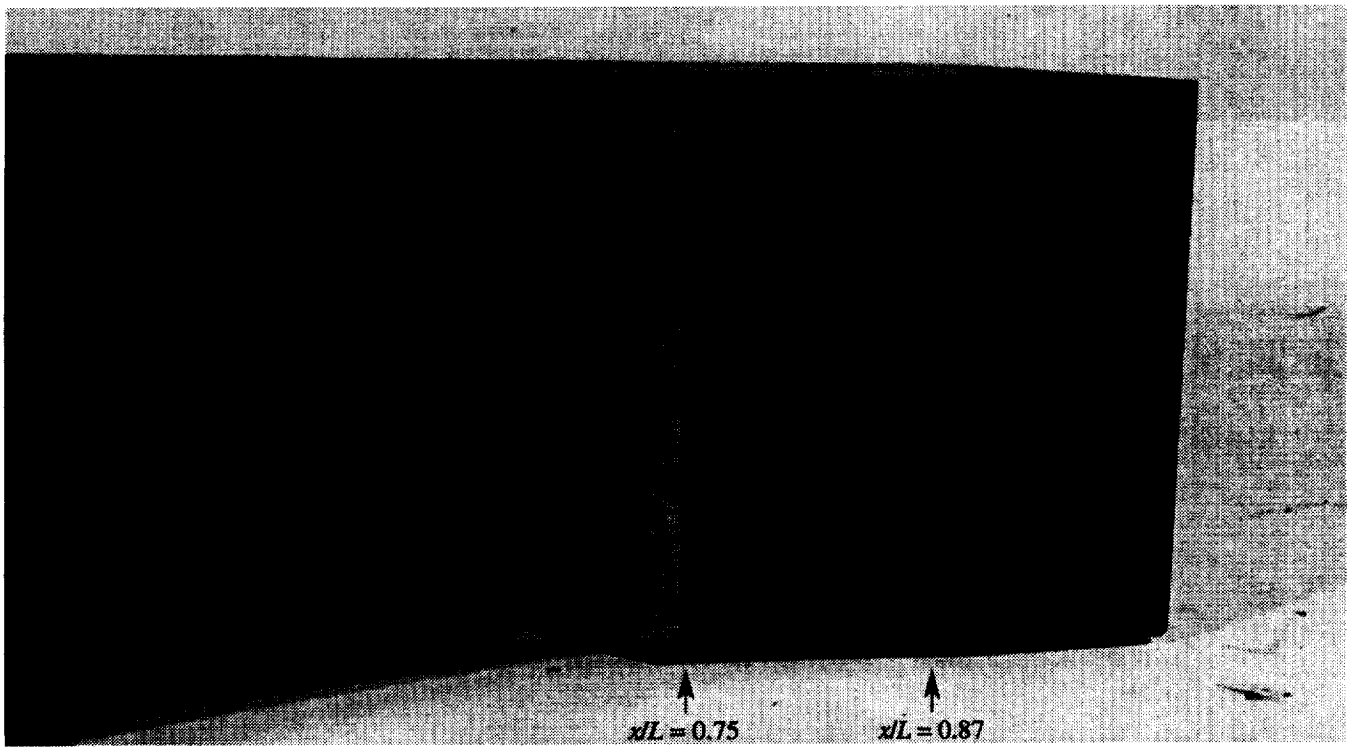

Figure 25. Streamline patterns along concave ramp, low Mach number nozzle at NPR = 13.

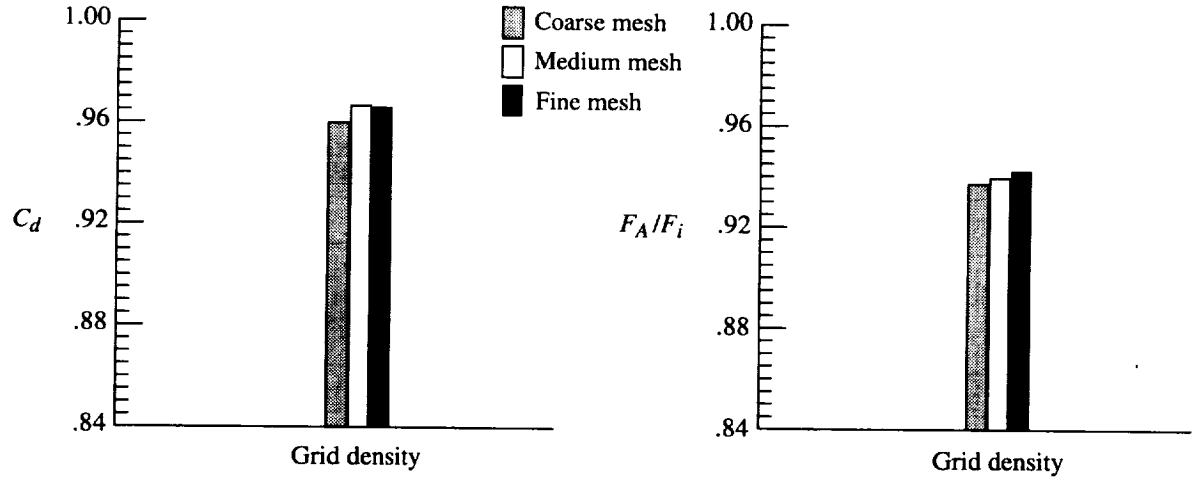

Figure 26. Effect of grid density on internal nozzle performance for concave ramp, low Mach number nozzle at $M = 0.05$ and NPR = 13.

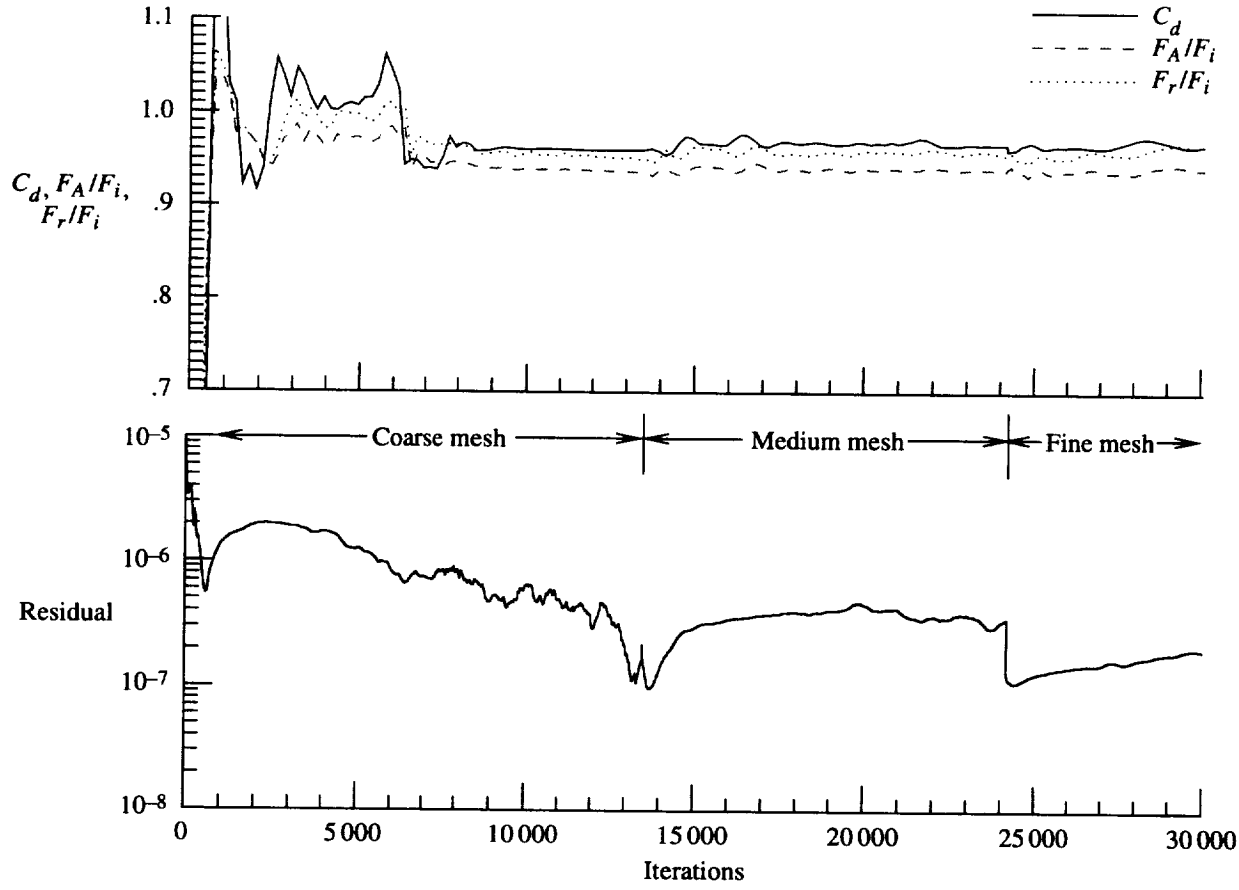

Figure 27. Solution convergence history for concave ramp, low Mach number nozzle simulation at $M = 0.05$ and NPR = 13.

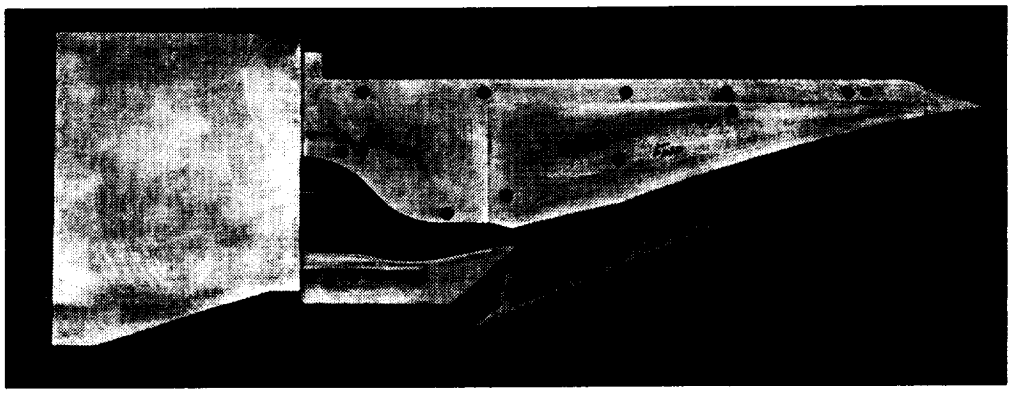

(a) Nozzle configuration with near sidewall removed and mounted to transition section.

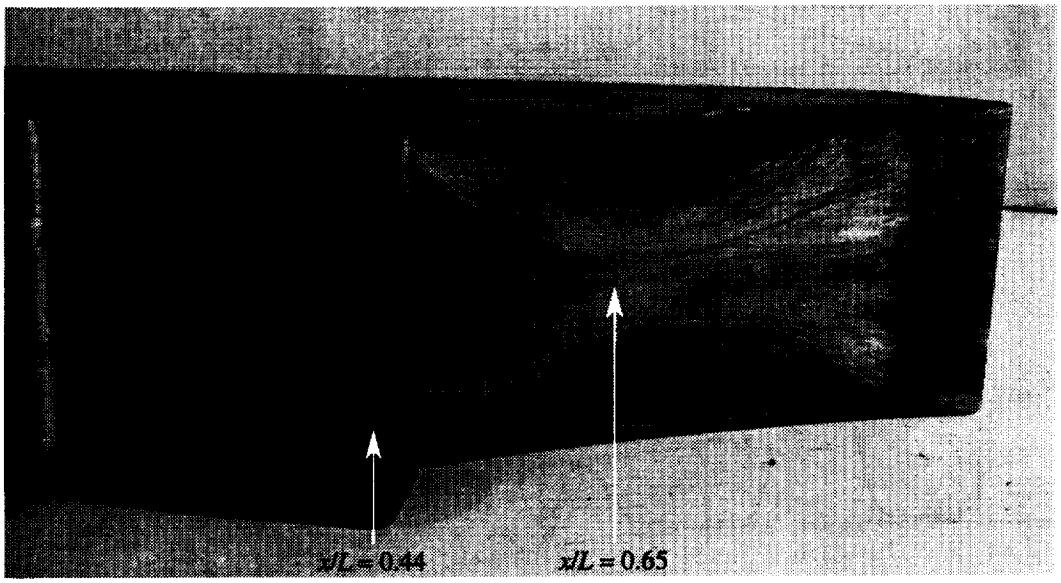

(b) Streamline patterns along concave expansion ramp at NPR = 13.

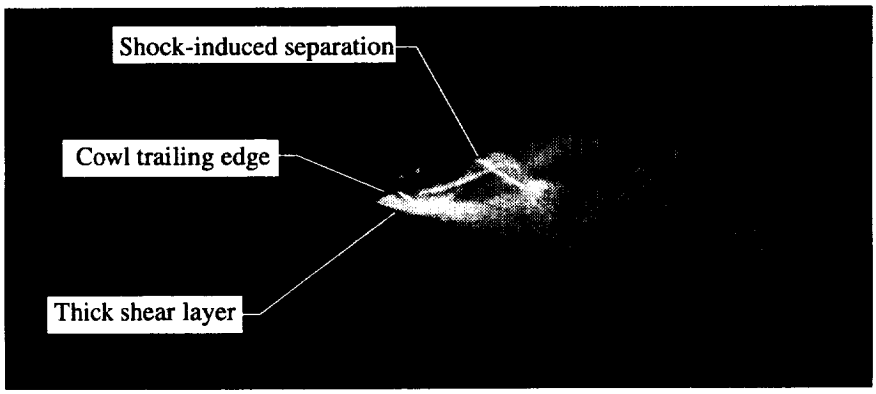

(c) Density gradients along nozzle centerline at NPR = 13.

Figure 28. Concave ramp, high Mach number nozzle.

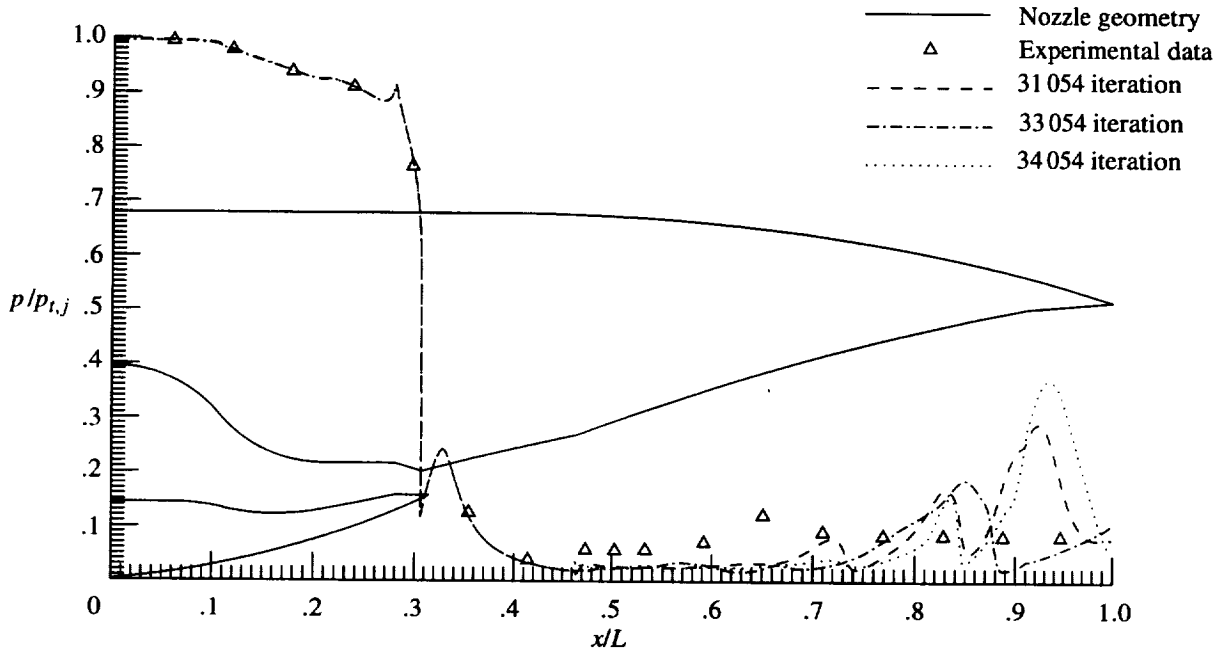

Figure 29. Predicted and experimental normalized static pressure distributions for concave ramp, high Mach number nozzle at $M = 0.1$ and NPR = 13.

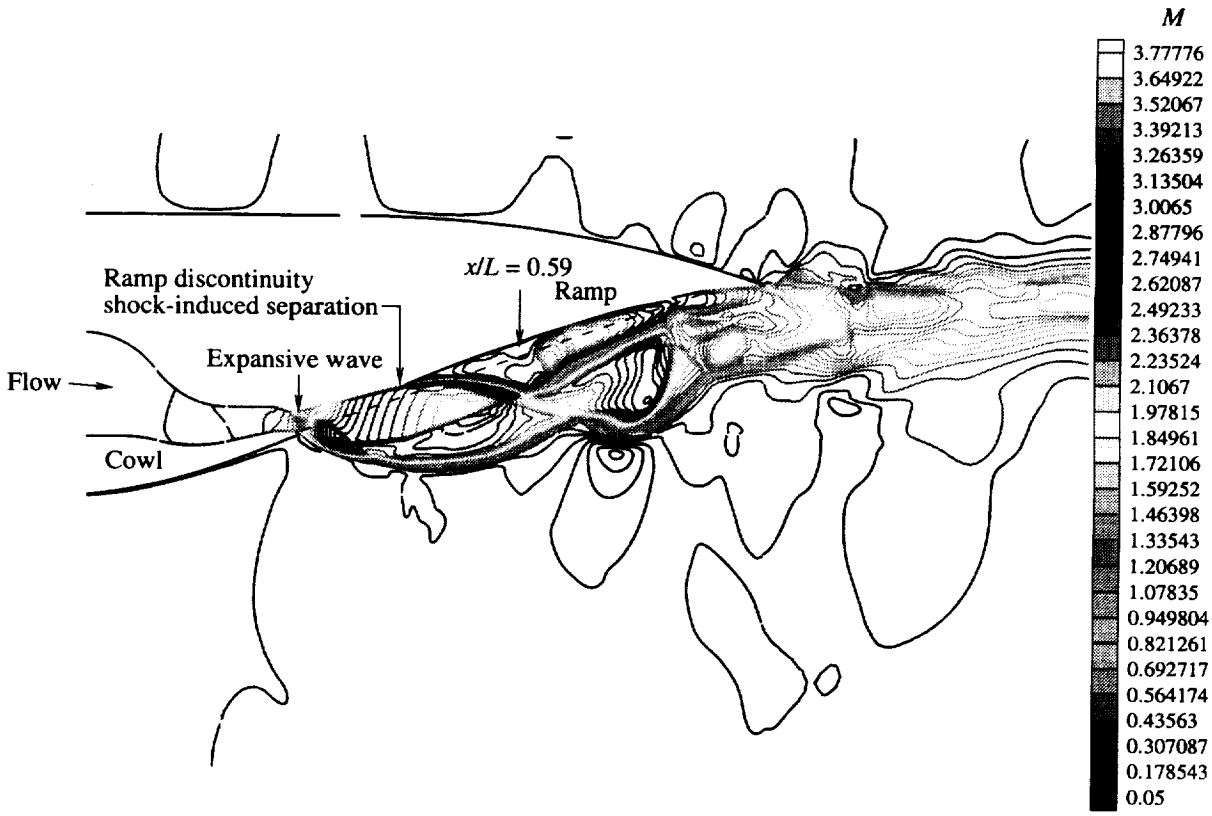

Figure 30. Predicted Mach contours along centerline of concave ramp, high Mach number nozzle at $M = 0.1$ and NPR = 13 for 34 054 iterations.

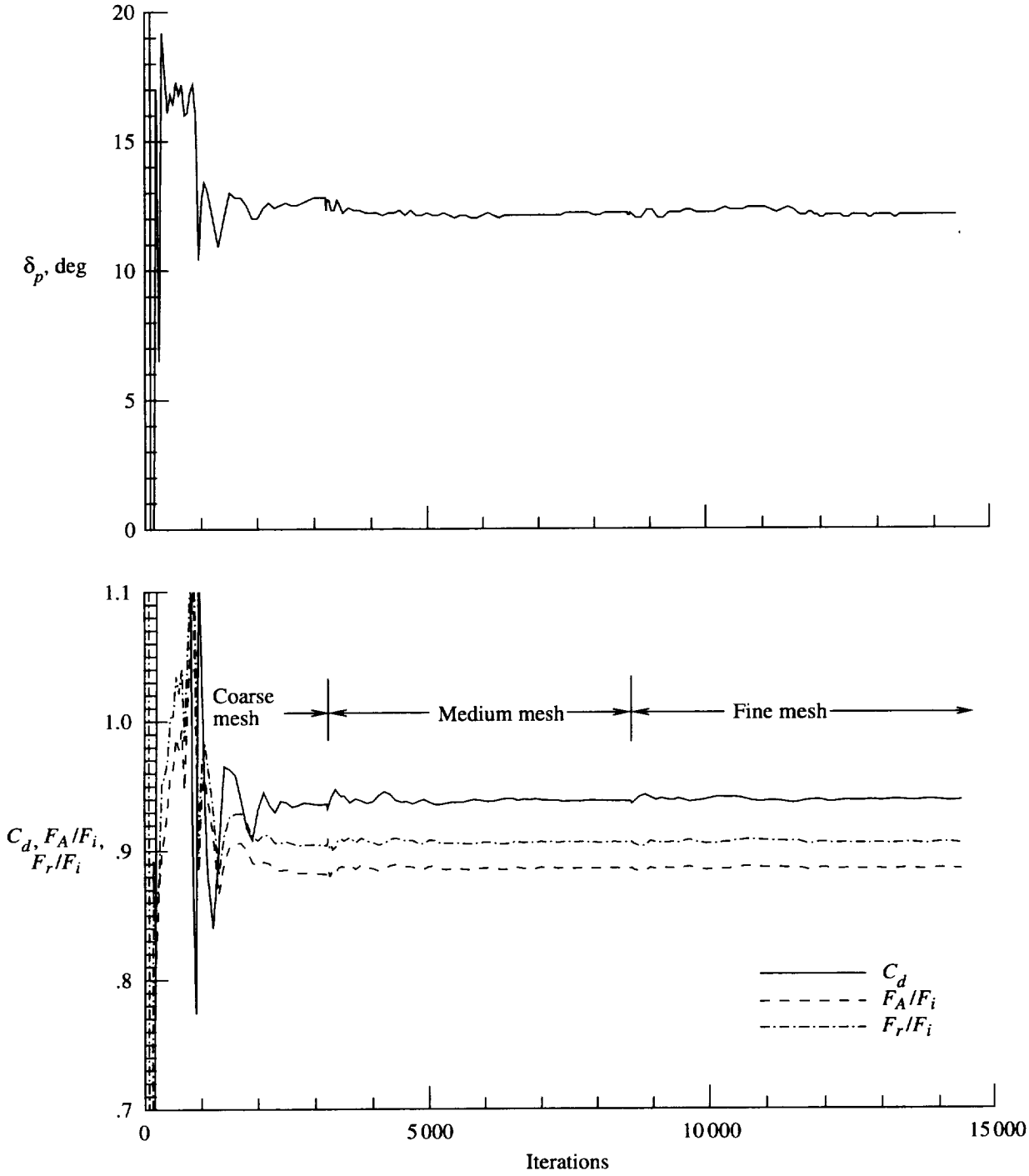

Figure 31. Solution convergence history for concave ramp, high Mach number nozzle at $M = 0.1$ and NPR = 102.

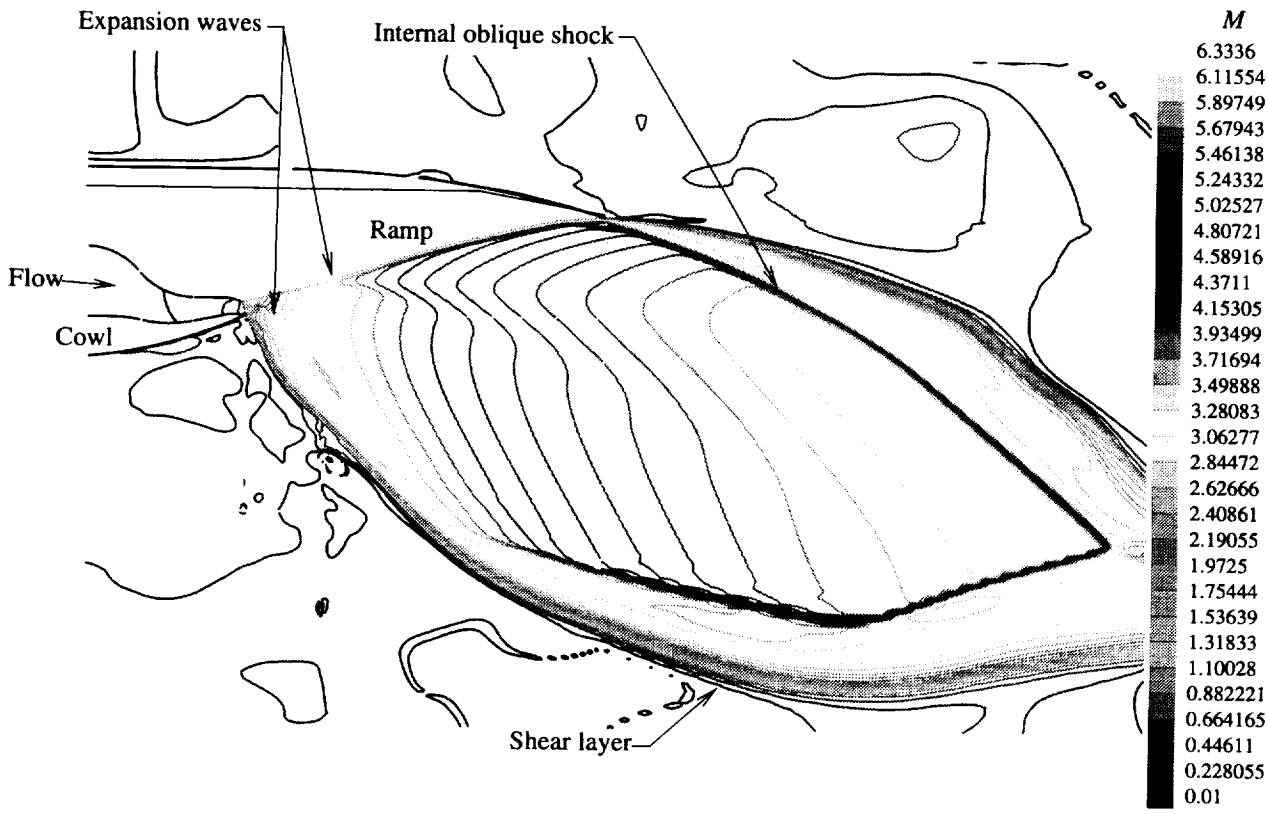

Figure 32. Predicted Mach contours along centerline of concave ramp, high Mach number nozzle at $M = 0.1$ and NPR = 102.

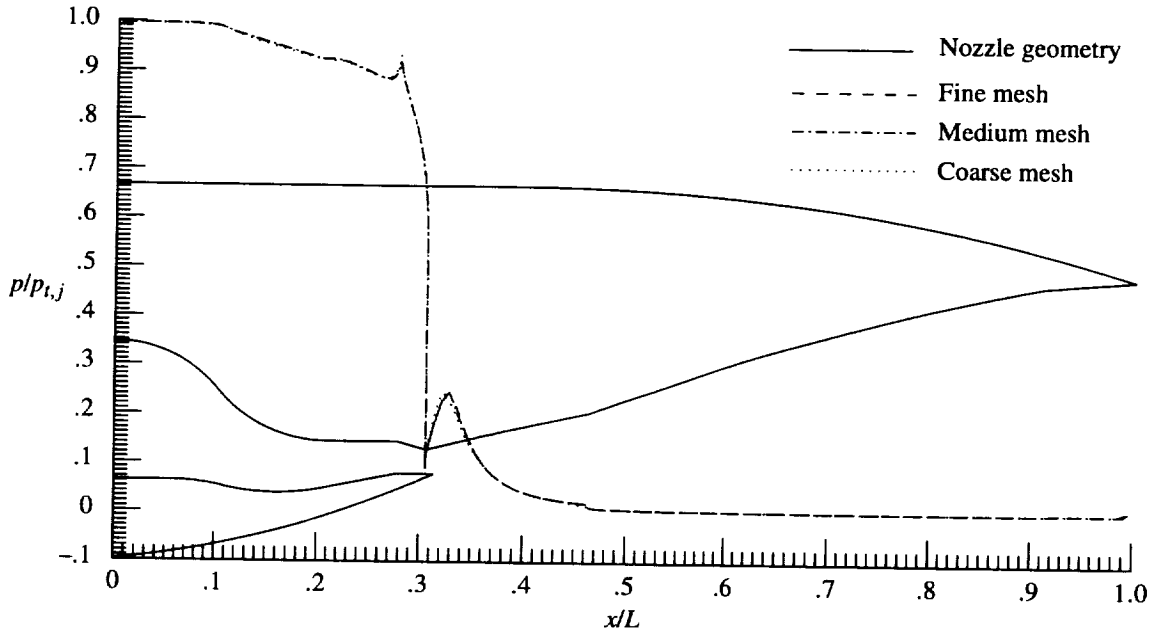

Figure 33. Predicted normalized static pressure distributions at each grid level for concave ramp, high Mach number nozzle at $M = 0.1$ and NPR = 102.